

Chapter 3

Photon Detectors for Small-Animal Imaging Instrumentation

Dieter Renker and Eckart Lorenz

1 Introduction

In nearly all detectors for small animal studies using the imaging technique, the first step in the detection of X-rays or gamma-rays (shortcut γ) is the conversion of the absorbed X-rays or γ 's into photons mostly in the visible spectrum by high z , high density scintillation crystals (see Chap. 1). In this process, normally only a small fraction of the absorbed X-ray or γ -energy is converted into light. Typical conversion efficiencies for commonly used scintillation crystals range between 20 and 100 eV energy loss for the generation of a single photon in the few eV range. As most scintillation crystals emit in the spectral range between 300 and 700 nm (with only a few exceptions) the typical conversion fraction in energy is between 0.1 and 0.02. Table 3.1 lists some parameters of common scintillation crystals, their peak spectral emission and the number of photons/keV deposited energy in that scintillation crystal. The numbers are typical values because many subtle effects can change the listed values, for example nonlinearities in the light emission as a function of the γ -energy or self-absorption losses of the scintillation material. For the physics of the main γ -absorption processes by the photoelectric effect or Compton scattering the reader is referred to Chap. 1.

After the conversion of high energy radiation into photons in the eV range the next processes are the photon transport to a photon detector and the conversion of the photons into an electrical signal by means of an optimally adapted photon detector. In the following we skip details of photon transport inside the crystals as well as

D. Renker (✉)
Paul Scherrer Institute, Villigen, Switzerland
e-mail: dieter.renker@ph.tum.de

E. Lorenz
Max Planck Institute for Physics, Munich, Germany
Eidg. Technische Hochschule, Zurich, Switzerland
e-mail: e.lorenz@mac.com

Table 3.1 Some key parameters of common scintillation crystals for X-ray and γ -ray detection

Scintillation crystals	Density (g/cm ³)	Atomic number Z	Photo fraction @ 511 keV (%)	Peak emission wavelength (nm)	Refractive index	Photons per keV	Decay time τ of main comp. (ns)	Hygroscopic
NaI(Tl)	3.67	43	18	410	1.85	38–40	250	Yes
CsI(Tl)	4.51	54		540	1.79	55	\approx 1,000	(Yes)
CsI(Na)	4.51	54		420	1.84		630	Yes
LSO ^a	7.4	65	34	420	1.81	27	40	No
LuI ₃ ^a	5.6	59		470		47	30	Yes
BGO	7.13	73	43	480	2.15	8	300	No
YAG	4.55	15		550	1.82	8	60–70	No
LaCl ₃ (Ce)	3.79	36		350	1.9	49	28	Yes
LaBr ₃ (Ce)	5.29	43	15	380	1.9	63	26	Yes

^aRadioactive

the problem of light extraction and efficient coupling of the scintillation crystals to the photon detector, referring the reader to Chap. 1 of this volume, and concentrate on the issue of the photon detection efficiency. Nevertheless, we make some simplifying assumption that only typically a fraction of light can be extracted and coupled to the photon detectors because of geometrical limitations.

While for CT detectors a high photon extraction efficiency is possible, the photon extraction efficiency in SPECT or PET detectors is typically only between 10 and 30 %, because one normally couples the photon detector to the rear cross section of the crystals. If intermediate light guides are used the extraction efficiency can be even lower. From the data in Table 3.1 a number of conclusions can be derived for the requirements for the photon detectors.

- The conversion of photons into photoelectrons should be as high as possible, i.e. the photon detector should have a high quantum efficiency (QE).
- The photon detection efficiency¹ (PDE), i.e. the efficiency to convert photons into measurable photoelectrons, should be close to the QE of the photon detector, i.e. losses of photoelectrons inside the photon detectors should be minimal.
- If the transfer of the photons from the scintillation location to the photon detector is inefficient, which normally is the case, and only a small fraction of the total number of produced photons impinge onto the photon detector, the requirements in high PDE in the detector will have to be even more demanding.
- Photons in the eV energy range can only be converted in common photon detectors into at most one photoelectron. Therefore the number of expected electrons from common scintillation crystals is much smaller than normally needed for data processing. Therefore signal amplification is needed. If possible, the amplifiers, either internal or external, should not degrade the signal.
- A timing signal in the (sub)-nsec range is frequently needed for PET but nearly all suitable scintillating crystals have a decay time in the range of 20–1,000 ns. In most cases only a few photons are emitted during the first (few) nsec(s) and could be used for deriving a timing signal. Therefore, suitable photon detectors require a good single photoelectron response (SER)
- It follows that for nsec timing measurements the photon detectors and the needed amplifiers (internally or externally) should have an intrinsic bandwidth equal to or superior to the goals in timing to be achieved.
- The spectral sensitivity of a photon detector should be optimally matched to the emission spectrum of the scintillation crystals.
- As scintillation crystals normally are of high refractive index (n in the range of 1.7–2.2) efficient optical coupling to the photon detector is needed.

¹It is quite common to use the QE to specify the number of photoelectrons in a photon detector. The QE ignores the subsequent losses of photoelectrons inside the photon detector, for example in the front-end of a PMT. The PDE, respectively effective QE specifies the more realistic number of photoelectrons that are amplified and processed in the subsequent electronics system following the photon converter of the photon detector.

It should be mentioned that both in PET and SPECT one normally tries to measure the time and energy of single γ -quanta with relatively high precision, while in CT one measures integrated fluxes and deposited energy as a function of time because the X-ray flux is normally much too high to allow counting and a measurement of the energy of individual X-rays hitting a detector pixel. A precise energy measurement of the individual X-ray quanta is currently not needed because of the broad energy spectrum of the X-ray generator and the lack of a method to determine the initial energy of X-rays before interaction in the body under examination. The γ -detectors for PET and SPECT should have at least an energy resolution of a few percent to separate the ' γ '-line from the Compton edge.

Also, some other conditions should be fulfilled for practical applications:

- The photon detectors should be unaffected by magnetic fields or at least be easily protected by suitable shielding materials.
- Nearly all devices for radiation detection normally work in an environment of high electromagnetic background. Therefore, a high immunity against EMI is needed.
- The devices must be easy to operate and should not drift over time in an uncontrolled way.
- Radiation damage is, in general, not an issue because most sensors were initially developed for other applications used in much higher radiation environments compared to that in small animal imaging devices.

Particularly for small animal imaging some requirements related to the small dimensions of the objects to be studied should be fulfilled:

- The resolution of the instruments should be well adapted to the dimensions of structures to be studied. This requires small pixel elements to achieve sub-mm resolution.
- As objects to be studied normally have dimensions comparable to the crystal length, parallax errors become important and need to be corrected.
- Scintillation crystals and particularly the photon detectors should be as compact as possible. This condition is a 'must' in case mobile applications are needed (see example in Fig. 3.17).
- As the volume to detector surface of a small animal PET is normally much smaller than in the case of a human PET the radiation levels will normally be smaller, simply because of the reduced uptake. Therefore, the timing resolution for separating events in PET and SPECT is less demanding than in human PET. Similarly, Compton scattering background inside the small animals is also much lower in small animal PET and SPECT compared to human PET/SPECT.
- In case of very compact detectors minimizing heat developed by the local electronics is an issue.

Currently, four families of photon sensors are used for fast, low light flux detection

- (a) Photomultipliers (PMT), i.e. vacuum photon detectors with secondary photo-electron multiplication by means of a number of dynodes at different electrostatic potentials.
- (b) Solid state photon sensors based on silicon without internal amplification:
 - PIN photodiodes, currently of very restricted use in PET or SPECT.
 - CCD arrays, only for CT.
 - Drift photodiodes
- (c) Solid state sensors, based on silicon, with internal amplification:
 - Avalanche photodiodes (APD) operated in the linear amplification mode just below breakdown voltage.
 - Geiger-mode avalanche photodiodes (G-APD) operated slightly above breakdown voltage but using avalanche induced current quenching following the Geiger principle
- (d) Exotic photon detectors.

There are quite a few special photon detectors (exotic photon detectors) allowing one in principle to detect low light level signals, such as for example hybrid photomultipliers, gaseous photon detectors, cryogenic photon detectors, or non-silicon solid state photon detectors. All these detectors have either severe deficiencies concerning the discussed application (large size, low QE, complex operation) or are not yet mature, respectively are not yet produced at large industrial levels.

PMTs are the long-term ‘workhorse’ for fast and low level light detection and are well established in the field of nuclear medical applications. Unfortunately, they are not suited to being operated in magnetic fields, such as inside Magnetic Resonance (MRI) scanners, and small pixel sizes are difficult to achieve. Nowadays, multi-anode PMTs with pixel sizes down to $2 \times 2 \text{ mm}^2$ are available. Equally suited for the readout of fine pixelated scintillating crystal matrices is the Anger-camera principle, i.e. the sharing of light from a pixel by a few larger area PMTs. While for human PET detectors the block detector principle is strongly favored because it allows for a large reduction in readout channels, a coupling of one photon detector to one crystal slab (1:1 coupling) is also possible for small animal PET detectors because the number of channels is still manageable.

The main deficiencies of APDs are their low gain, their sensitivity to temperature changes and to even small voltage drifts, all of which are difficult to control. It is quite likely that the use of linear mode APDs is only an intermediate step towards the use of G-APDs as readout elements in the near future. G-APDs are still under development, but rapidly approaching maturity. They offer a number of advantages making them the most promising photon detectors in PET/SPECT for small animal imaging.

Before discussing the different sensors in detail we present in Table 3.2 a comparison of the advantages and disadvantages of the PMTs, APDs and G-APDs for the use in PET and SPECT detectors using scintillation crystals as γ -detectors.

Table 3.2 Comparison of some basic features (typical) of PMTs, APDs and G-APDS for PET and SPECT crystal readout. Some parameters are expected to improve in the near future^a

Feature	PMT	APD	G-APD
Volume, compared to crystals	<i>Very large</i>	Very compact	Very compact
Readout Pixel structure	<i>Limited</i>	Very fine	Very fine
Block readout	Well established	First tests	First tests
Area limitations	No	Few cm ²	<1 cm ²
User experience	High	Some	Prototype
Costs	Very high	Medium	Still high, long-term lowest
Operation voltage (V)	<i>1,000–1,500</i>	300–500	30–100
Voltage regulation needed	High	<i>Very high</i>	High
Gain	10 ⁵ –10 ⁶	<i>50–300</i>	10 ⁵ to few 10 ⁶
Dynamic range	High	High	Some limitations
High rate operation	High	<i>Limited</i>	Minor limitations
Sensitivity to magnetic fields	<i>Very high</i>	No	No
Need for high quality preamp	No	<i>Yes</i>	No
Sensitivity for pick-up	Medium	<i>Very high</i>	Low
Requirement for shielding	Some	<i>Necessary</i>	Optional
Quantum efficiency (%)	20–25	60–80	25–50
Can detect single photons	Yes	No	Yes
Pulse risetime single photoel.	1–2 ns		<1 ns
Noise	Very low	High	High, uncritical
Excess noise factor	1.2–1.5	<i>5–10 at gain 1,000</i>	1.0–1.2
Temperature sensitivity	Very low	Very high	Medium for high overvoltage
Sensitivity to bias drifts	Low	Very high	Medium for high overvoltage
Commercially available	Yes	Yes, new	Yes
Damage due to light exposure	High	No	No
Radiation damage	Modest	Low	<i>Modest</i>
Potential for mass production	<i>Low, hand assembled</i>	Medium, ion implantation	Very high, CMOS technology

^aIn italics: parameters that can seriously affect performance

The structure of the section on photon detectors is the following: in Sect. 2 we will briefly review the general principle of photon detection. In Sect. 3 we will give a short survey of the processes influencing the signal losses from the conversion in the crystal to the detection of the photons in the photon detector influencing the energy resolution and timing. In Sect. 4 we will discuss the classical photon detector, the photomultiplier, reviewing its basic design principle, features and limitations. In Sects. 5 and 6 we will discuss solid state photon detectors without and with internal gain, their basic construction and their features and limitations relevant for photon detection in small animal imaging. Also in Sect. 6, we will briefly mention some application examples, while in Sect. 7 some special requirements not specific

to photon detection will be discussed. In Sect. 8, a short outlook on prospects on improving photon detection in the future will be given. It should be mentioned that in this report emphasis is mainly put on more recent photon detector developments, which are at present mostly driven by the requirements for PET or SPECT. In particular, we will only briefly mention their uses and details in CT because the photon detection technology in this area is rather static since a few years and well documented. On the other hand, the solid state photon detectors, based on the Geiger mode avalanche photodiodes (G-APD), are given more room, because these detectors are undergoing rapid progress and have the potential of becoming soon the leading photon detector for scintillation crystal readout in small animal PET. It is perhaps interesting to mention that at the recent photon detector conference in Aix-les Bains (2008) more than half of the submitted contributions were dealing with developments of G-APDs.

2 Some Comments on Resolution Issues

Before discussing details of the photon detectors we will briefly discuss some issues concerning resolution requirements. Emphasis is again put mostly on PET and SPECT.

In small animal imaging instruments using radiation detectors, one has to deal with three issues of resolution² linked in part to the photon detectors:

- The spatial resolution,
- The energy resolution,
- The timing resolution.

The spatial resolution is mostly influenced by the geometry and crystal subdivision of the detector. In case of a geometry with a 1:1 coupling the energy resolution and noise contribution of the photon detector has very little impact on the image resolution, except an uncertainty of the depth of interaction (DOI) in PET, resulting in a parallax error along the crystal length. In principle, one is able to measure the DOI by means of a readout from both crystal ends and a comparison of the pulse heights. Other methods consist of combining two shorter crystal slabs of very different decay time to a longer slab thus allowing one to tag the interaction in one of the two sections by pulse shape discrimination. A high energy resolution as well as a good pulse shape measurement will reduce false associations. The situation is quite different in the block detector readout. Here, the energy resolution and the contribution from the detector noise can influence the image resolution.

In the following we use the example of PET to demonstrate the limitations and benefits of standard photon detectors concerning the image resolution.

²Here we follow the convention in nuclear medical applications for the definition of the resolution as the FWHM ($\text{FWHM}=2.35 \sigma$) of the distribution.

Moses and Derenzo proposed an empirical formula, which nicely describes the reconstructed FWHM spatial resolution [2]:

$$FWHM = a\sqrt{(d/2)^2 + b^2 + r^2 + (0.0022D)^2}$$

where d is the detector size, b the position decoding accuracy, r the positron range, D is the system diameter used to describe the photon annihilation non-colinearity, a is a correction factor and depends on the algorithm used to reconstruct the images a ranges typically from 1.1 to 1.3.

The photon non-colinearity is almost negligible in a scanner for small animals and the positron range r is given by the isotope used, while d and b can be minimized in the design. In case of installing the PET detector inside a high field MRI magnet, the range of the positrons is shortened by ‘spiraling’.

“Block” detectors using light sharing and Anger-like logic, the only choice when standard PMTs are used, have in average a value $b \sim 2$ mm [3–7]. A better value of $b \sim 1$ mm can be achieved with 1:1 direct coupling of crystals to position-sensitive or multi-anode PMTs [8–13].

Only the third category, where the crystals are individually coupled to photon detectors and independent electronics, achieves an intrinsic resolution that is equal to the geometric resolution ($b \sim 0$) [14–17]. This readout scheme can be currently only realized with solid state photon detectors which can be tailored to the required geometry. An image resolution of 1 mm has been achieved with 0.8 mm wide crystals [18].

The energy resolution is of less importance provided one is able to separate the photopeak events from the Compton events. The energy resolution is influenced by quite a few different processes, which can eventually prevent a clear separation of the photopeak from the Compton edge. In the following we assume for simplicity that we deal with only 511 keV γ -quanta, which are fully absorbed in a single crystal slab. The following processes will all contribute to a degradation of the energy resolution:

- (a) The scintillation light yield will depend on the local ‘quality’ of the crystal, i.e. from the local crystal defects and local admixture of activation material.
- (b) A small but important broadening of the resolution will be the so-called non-proportionality of the light yield at very low γ or electron energies. This effect is strongest at lowest energies and broadens the intrinsic scintillation resolution beyond the $2.35/N$, N being the mean number of scintillating photons. A very good scintillation crystal, such as YAP:Ce or LaCl₃:Ce can have an intrinsic energy resolution of around 5 % at 511 keV.
- (c) The next process in broadening the scintillation photon distribution seen from an end of the crystal is the variable light collection influenced by geometrical effects, absorption losses inside the crystal, surface scattering losses and effects of the reflector material (diffuse reflection, specular reflection). In case of a truncated pyramid shape of the crystals in a radial arrangement and a readout by

the rear crystal end one can easily get a higher light yield from the far side than from the side of the readout. This results in a broadening of the resolution when averaging over the crystal. By appropriate surface treatment it is possible to improve the uniformity and in turn the resolution. Generally one can collect at most 25–50 % of all photons in a not too long crystal at the rear surface to be coupled to a photon detector. In case of long crystals these numbers will significantly decrease.

- (d) At the end-face one normally couples the crystal to the photon detector by means of optical grease or optical glue matched closely to the refractive index of the PMT glass window or the silicon photon detectors, which are normally protected by a thin layer of transparent plastic material. As most useful crystals for PET or SPECT have a refractive index well above the optical coupling material, a sizeable fraction of the light remains trapped inside the crystal.
- (e) The next class of loss is the backreflection of photons by the photon detector, which in case of a PMT can vary between a few percent to up to around 30 % (wavelength dependent). Also silicon photon detectors have quite some backreflection. Part of the backreflected photons might be ‘recycled’ a second time onto the photon detector in case of small and compact crystals while for long crystals most of the backreflected photons are lost.
- (f) Not all the photons entering either the photocathode in a PMT or the silicon of the silicon photon detectors are converted into free electrons. The relevant number is the quantum efficiency (QE), which is the ratio of the number of ‘freed’ photoelectrons to the number of impinging photons. Typical QE values for classical PMTs range between 20 and 30 % at peak sensitivity, close to 80 % for PIN and avalanche photodiodes and anywhere between 20 and 70 % for G-APDs (depending of the active to total area ratio, often called the fill factor).
- (g) Not all the photoelectrons can be collected and amplified. It is therefore more appropriate to replace the QE by the so-called photon detection efficiency (PDE). The ratio of the PDE/QE has typical values between 0.8 and 0.9 for the best PMTs³ (≈ 0.6 – 0.7 for mesh dynode PMTs, due to geometrical effects), close to 1 for PIN and avalanche photodiodes and between ≈ 0.2 and 0.6 for current G-APDs (strongly dependent on operation parameters).
- (h) The amplification normally adds some additional broadening of the resolution distribution on the amplified photoelectrons. This number is commonly named the excess noise factor F (see Sect. 4.4). Best PMTs have an F -factor of 1.1–1.2, PIN photodiodes an intrinsic F factor of 1 (plus the intrinsic noise contribution from the amplifier), linear mode APDs have a typical F -factor ranging from 5 to 10 at a gain of 500 (see Fig. 3.13) with a very strong gain dependence while G-APDs have a value of about 1.1–1.3, again gain and geometry dependent.

³There exists another source of loss in the PMT front-end. Photoelectrons are sometimes backscattered when impinging on the first dynode and have a very low chance to produce a secondary electron. This process is up to now not well measured and often ignored.

In the above list we ignored small effects like trapping effects, phosphorescence or wavelength shifting, etc.

It is obvious that due to the multitude and diversity of processes affecting the energy resolution it is difficult to predict the resolution beforehand. Monte Carlo simulation might predict the resolution within 30 %. Experimental optimization is currently the most frequently used procedure to determine the resolution. For example, single LSO crystals coupled to selected PMTs can give about 10 % resolution for 511 keV γ s, while one normally achieves a resolution of 12–25 % in densely packed arrangements and a block readout. At around 25 % resolution one already has considerable overlap between the photopeak and Compton events.

As mentioned before, timing resolution in the 0.5–1 ns range is in most cases sufficient, because it is very difficult to achieve high counting rates in small animals due to the limited uptake.

As nearly all scintillation crystals, except a few unsuited materials such as ZnO or the J9758 from Hamamatsu, have quite long decay times, one generates timing signals from the very first detected photon respectively from the rise time of the scintillation pulses by using standard methods, such as constant fraction discriminators, leading edge discriminators, or the high-low discrimination technique. As the crystals are normally only a few (10–20) mm long, time dispersion inside the crystal can be ignored.

A reason for generating timing signals is the need for coincidence triggers from the two gammas. With PMTs and G-APDs it is possible to achieve sub-ns time resolutions, while photodiodes and avalanche photodiodes allow only a considerably worse timing resolution of, at best, a few ns.

A good pulse shape discrimination is essential for DOI measurements when combining two scintillation crystals of a different decay time.

3 General Principle of Photon Detection

Two processes, the external and the internal photoeffect, are used for the detection of photons. Both are based on the transfer of the photon energy to an electron in a collision. When a photon impinges on the surface of any material it can liberate an electron, provided the energy of the photon is higher than the photoelectric work function ϕ . This was first formulated by A. Einstein in 1905 [1]:

$$W_{kin} = h\nu - \phi$$

The kinetic energy W_{kin} of the electron can be sufficient to bring the electron not only from the surface, but also from the volume of the material, to the free space. Semiconductors have a very small work function ϕ . Consequently, the threshold wavelength of the incoming photon can be in the near infrared. Standard alkali photocathodes in photomultipliers (Sb–Rb–Cs, Sb–K–Cs) have a threshold at 630 nm (red light).

The internal process needs less energy. In a semiconductor it is sufficient to lift an electron from the valence band to the conduction band. Therefore a silicon crystal (bandgap 1.1 eV) can be a very efficient photon detector in the complete range of visible light. If the electron does not recombine with the hole in the conductive band due to the electric field of a silicon photodiode it can be collected and the signal amplified.

4 Classical Readout Using PMTs

4.1 History

In 1913, Elster and Geitel invented the first photoelectric tube. Some years earlier, in 1889, they had reported the photoelectric effect induced by visible light striking an alkali metal [19]. The first photomultiplier tube (PMT) was invented in 1930 by L. Kubetsky. In 1939, V. Zworykin and his colleagues from the RCA laboratories developed a PMT with electrostatic focusing [20], the basic structure of current PMT's (Fig. 3.1). A short time afterwards it became a commercial product. Single photons were detectable from now on.

Further innovations have led to highly sophisticated devices available nowadays. The bulky shape turned into a flat design with a length of a few centimeters and with pixilated anodes the PMTs became position sensitive. While early PMTs allowed only a block readout, a 1:1 coupling of crystals to a position sensitive PMT became possible, a scheme where the end faces of small crystals are coupled to a matching pixel of the PMT (Fig. 3.2). A vacuum container is still needed, but the fraction of the active faceplate area compared to the total faceplate of the PMT is now close to 90 %.

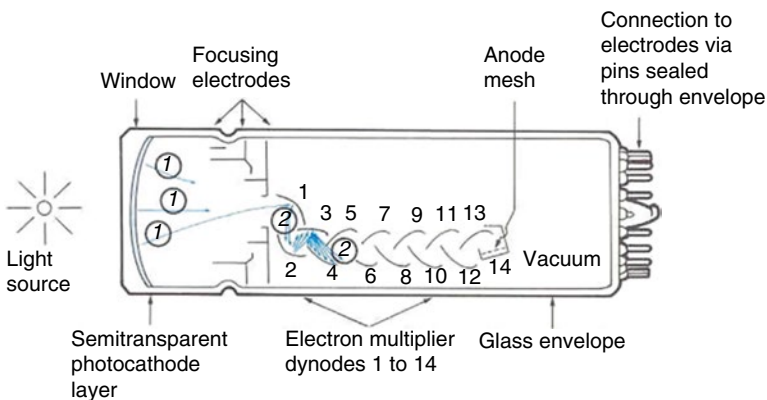


Fig. 3.1 Cross section of a photomultiplier tube. (1) Indicates the electrons liberated by photons from the photocathode and (2) shows the cascade of secondary electrons in the first stages of the multiplier dynodes

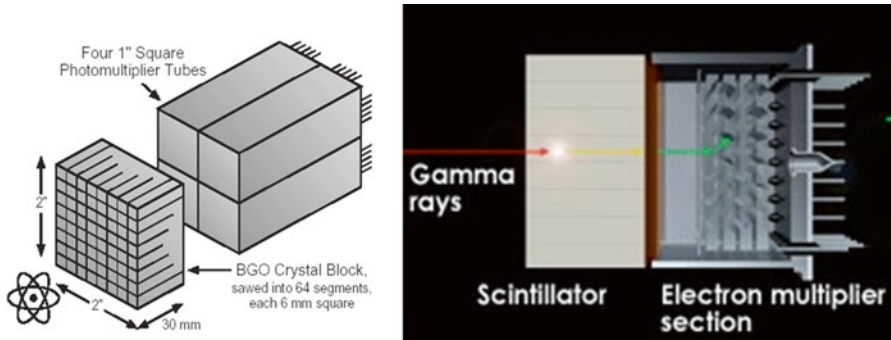


Fig. 3.2 Crystal block design with conventional PMTs (*left*), and 1:1 coupling with state of the art position sensitive flat panel PMTs (*right*). Shown are the small scintillating crystals and the individual dynode structure and anode of the PMT pixels

4.2 Gain

The gain of standard PMTs is very high with typical values of 10^6 – 10^7 . It is almost completely independent of the temperature and in a wide dynamic range independent of the rate that needs to be handled. Without the need for an amplifier the output signals can be directly fed into standard readout electronics.

4.3 Photon Detection Efficiency

The main characteristic of a photomultiplier is its quantum efficiency (QE), which describes the probability of a photon creating a free electron, which can be amplified in the dynode structure. Several effects influence the QE: the photon can be reflected by the glass of the window, it can pass through the photocathode without interaction and it can produce an electron in the volume of the photocathode which electron is stopped inside the material. The overall effect limits the QE to typically 25 %. Manufacturers usually provide the radiant sensitivity (the cathode photocurrent divided by the radiant power), not the QE. An example is shown in Fig. 3.3.

As can be seen from Fig. 3.3, it is possible to select a photocathode material, which matches the emission wavelength of the crystal scintillator used.

The QE can be calculated from the radiant sensitivity $S_k(\lambda)$ by

$$QE = S_k(\lambda) \cdot \frac{hc}{e\lambda} \Rightarrow QE(\%) = 1.24 \cdot \frac{S_k(\lambda)}{\lambda}$$

with the Planck’s constant h , the speed of light c , the wavelength λ expressed in nm and $S_k(\lambda)$ in mA/W.

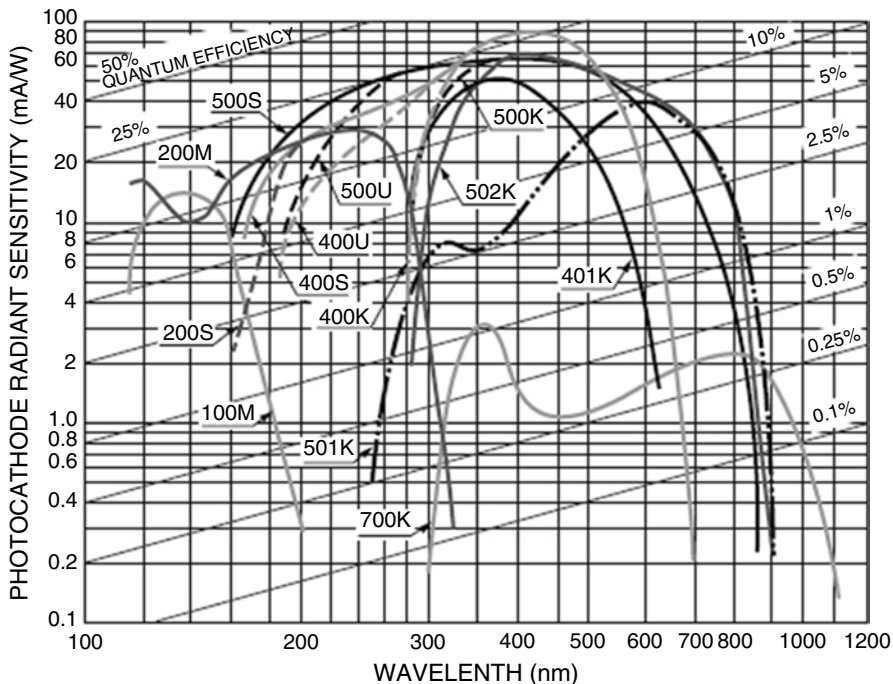


Fig. 3.3 Radiant sensitivity for several photocathode materials. The QE is indicated by the inclined lines (Hamamatsu PMT handbook)

Recently, the QE was boosted to values above 40 % by employing extremely pure bialkali photocathode materials and precise control of the vapor deposition process [21]. Photocathodes made of GaAsP(Cs), a new material, which is difficult to deposit, also provides a QE of more than 50 % in a wide range of wavelengths.

Usually the collection efficiency (CE), i.e. the probability that an electron, liberated from the photocathode, reaches the first dynode, is neglected. The CE can be as low as 70 %. The photon detection efficiency (PDE), the probability of an incoming photon creating an output signal is:

$$PDE = QE \times CE$$

Actually, some other effect might further reduce the PDE, even if the photoelectron hits the first dynode. Depending on the dynode material and the acceleration voltage, the photoelectron might, with some probability, be backscattered (elastically or inelastically) and will thus not produce any secondary electrons at all or only a few. Backscattering is not fully understood and is normally treated as part of the collection efficiency.

Hybrid photon detectors are a variant of the photomultiplier. The vacuum container and the photocathode are the same, but multiplication is not realized in a

chain of dynodes. The electrons liberated in the photocathode by a photon are accelerated in a high electric field (15–25 kV) and are focused onto a silicon diode or onto an avalanche photodiode (APD). In the silicon, the electrons lose their energy by ionization. They produce electron–hole pairs, which can be collected in case they are produced in the depletion layer. The diodes (avalanche diodes) need a very thin p⁺(n+) top layer, because the pairs created in this layer recombine immediately and are lost. An energy loss of 3.6 eV is needed to create an electron–hole pair. The ratio of the gained electron energy (corrected by the loss in the dead area) divided by 3.6 eV sets the amplification, which is about 5,000 when using a PIN diode while in case of an APD this has to be multiplied by the APD internal gain (resulting in a total gain of a few 10⁵–10⁶).

4.4 The Excess Noise Factor

The energy resolution $\sigma(E)/E$ of a crystal-PMT assembly is dominated by the stochastic distribution of the produced and collected photons (N_{photon}).

$$\frac{\sigma(E)}{E} = \sqrt{\frac{1}{N_{\text{photon}} \cdot PDE}}$$

The resolution is degraded by the excess noise factor F, which is mainly caused by the secondary electrons produced in the first dynode. The resolution becomes:

$$\frac{\sigma(E)}{E} = \sqrt{\frac{F}{N_{\text{photon}} \cdot PDE}}$$

A typical value is $F \approx 1.2$ for standard PMTs (The character F is also used for the Fano factor which affects the photon statistics or the statistics of electron–hole generation in semiconductors and is used in Sect. 2. In the light production in scintillating crystals, Poisson statistics apply and the Fano factor is $\cong 1$).

4.5 Time Resolution

The output signal of PMTs is very fast (rise time of about 1 ns) provided the proper dynode structure is used. In such cases it is possible to achieve an excellent time resolution, which is limited by the so-called transit time spread (TTS). This is a measure of the variations of time an electron needs for travelling from the photocathode to the first dynode. Typical values are about 200 ps. Some PMT types, in which mesh dynodes or micro channel plates are used as electron multipliers, show a very small TTS, and a time resolution of only 50 ps or even less can be achieved. The caveats of such structures are a higher price and a reduced CE.

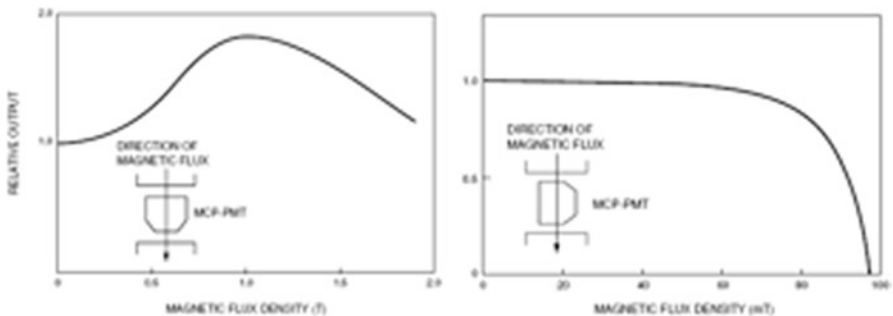


Fig. 3.4 Relative output of an MCP–PMT when its axis is oriented parallel (*left*) and perpendicular (*right*) to a magnetic field

Besides the transit time spread, some PMTs also show different delay effects of photoelectrons emitted in the central area and those emitted at the outer area because of the longer flight path and in turn lower field strength when focusing photoelectrons onto a small dynode area.

Like the energy resolution, the time resolution improves in first order with the number of detected photons:

$$\sigma(t) \propto \sqrt{\frac{1}{N_{\text{photon}} \cdot PDE}}$$

4.6 Operation in Magnetic Fields

Both normal and hybrid PMTs, are extremely sensitive even to small (mT) magnetic fields. Specialized devices with micro channel plates (MCP) instead of the dynode structure work in magnetic fields, but only if it is strictly parallel to the axis of the PMT (Fig. 3.4).

4.7 Advantages and Disadvantages

For many decades, PMTs have been the workhorse for single photon and low level light detection. Their advantages are obvious:

- The gain is high (10^6 – 10^7) and in most cases no amplifier is needed.
- The operation is relatively stable because the temperature dependence of the gain is very small. Nevertheless, some gain drift can occur, particularly immediately after biasing.

- A very good energy resolution can be achieved when state of the art scintillating crystals are used (i.e. lutetium–oxyorthosilicate or the newly developed $\text{LaCl}_3(\text{Ce})$ or $\text{LaBr}_3(\text{Ce})$ crystals).
- Compared to most other photon detectors the excess noise factor is small.
- An excellent time resolution can be obtained.
- The multiplication in a chain of dynodes is one of the best known low noise amplifications.

There are a number of disadvantages:

- Most severe is the strong sensitivity to magnetic fields (preventing any use in MRI magnets).
- PMTs need a high operating voltage of about 2 kV and special devices (hybrid PMTs) need about 20 kV.
- State of the art PMTs have a peak QE of typically 25 % and a typical front-end photoelectron collection efficiency of 70–80 %, i.e. a peak PDE of around 20 %.
- It is very difficult to produce a very fine pixilated ($<2 \times 2 \text{ mm}^2$) PMT.
- State of the art PMTs have rather large volumes compared to the crystals commonly used in small animal detectors. It is therefore difficult to build high resolution detectors with a 1:1 coupling.
- It is impossible to stabilize the gain by some feedback mechanism like in operation amplifiers
- The fabrication of PMTs is costly because 30 or more parts have to be assembled by hand in a vacuum container which afterwards has to be well sealed.

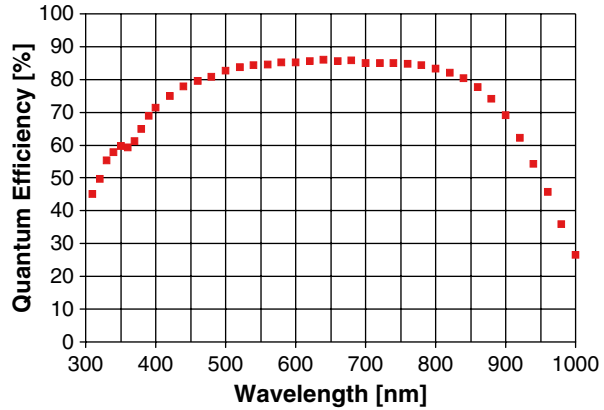
5 Readout with Solid State Photo Sensors Without Internal Gain

5.1 History

Semiconductor photodiodes were developed in the early 1940s approximately at the time when the photomultiplier tube became a commercial product. Only in recent years, with the invention of the Geiger-mode avalanche photodiodes, semiconductor photon detectors have reached a sensitivity comparable to that of photomultiplier tubes. The evolution started in the 1960s with the p-i-n (PIN) photodiode, a very successful device, which is still used in many detectors for high energy physics and in a large number of other applications like radiation detection and medical imaging. The next step was the development of the avalanche photodiode (APD), leading to a substantial reduction of noise but not yet achieving single photon response.

The weakest light flashes that can be detected by the PIN diode need to contain several hundreds of photons. An improvement of the sensitivity by two orders of magnitude was achieved by the development of the avalanche photodiode, a device

Fig. 3.5 QE as function of the wavelength of a silicon photodiode. Reprinted with permission from [22]



with internal gain. At the end of the millennium, the semiconductor detectors evolved with the Geiger-mode avalanche photodiode into highly sensitive devices, which have an internal gain comparable to the gain of photomultiplier tubes and a response to single photons.

Solid state devices have the big advantage that they can be produced in standard fully automated processes and can therefore be cheap. They can be customized to individual needs in a short time, i.e. within few months, they have low mass and very small space consumption, and they need only a low operating voltage. The detector by itself is only about 0.3 mm thick, and the housing thickness can be less than 0.5 mm. In addition, they are insensitive to magnetic fields with a theoretical limit of about 15 T. The quantum efficiency is very high in all solid state devices, because basically only the reflection at the surface reduces the detection probability. A silicon photodiode has a QE of 85 % in almost the whole range of visible light [22]. In the blue range of the spectrum, where most scintillating crystals have their peak emission, the QE is still 70–80 % (Fig. 3.5). It is difficult to achieve a high QE below ≈ 400 nm because of the very short absorption lengths of UV photons.

5.2 Detectors Integrating Over Many Photons

In detectors integrating over many photons (subsequently called integrating detectors) the signal is proportional to the number of photons per time interval. Integrating light detectors nowadays are mostly found in image processing for consumer or medical applications. Best known are simple versions, called Charged Coupled Devices (CCD), which can be found in digital cameras as well as in highly sophisticated devices in astronomical telescopes or as X-ray detectors on satellites. CCDs made of an array of pixels have a quantum efficiency of 70 % and more over a rather wide spectral range, making them far more sensitive than photographic films, which capture only about 2 % of the incident light.

Faster, cheaper and less power-consuming are the Monolithic Active Pixel Sensors (MAPS) or Complementary Metal Oxide (CMOS) image sensors, which, in contrast to CCDs, are compatible with the Complementary Metal Oxide production technology. All components necessary for the readout can be implanted on one single piece of silicon.

In hybrid pixel detectors, a pixelized sensor chip made of any kind of semiconductor material is bump-bonded to a readout chip. Photon detection with this technique is only possible when the photon energy exceeds several keV. In imaging applications, the hybrid pixel detectors define the incident radiation through the counting of the radiation quanta in every pixel [23].

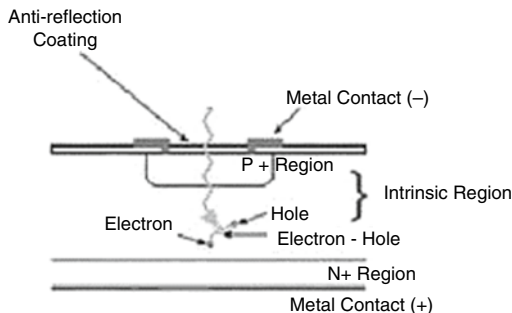
For radiography, the MEDIPIX (versions 1, 2 and 3) chip [24] and the MPEC chip [25] have been developed. These chips can be combined with sensors made of various semiconductor materials including the high-Z material CdTe.

The first large-scale hybrid pixel detector in operation is the PILATUS detector [26], developed at the Paul-Scherrer-Institute in Switzerland for proton crystallography experiments like at the Swiss Light Source (SLS). A remarkably low energy threshold below 3 keV has been obtained with 320 μm thick Si sensors [27]. PILATUS is a modular system. Each module consists of a Si sensor bump-bonded to an array of 8×2 chips using indium balls. It has 487×195 pixels with a pixel size of 0.172 mm. The 16 chips of a module are read out in parallel within a read-out time of ~ 2 ms. The PILATUS 6 M contains 6×12 modules, spans an area of 424×435 mm² and has six million pixels in total. With thin (20 μm) YAG(Ce) or LuAG(Ce) scintillating screens coupled to CCD cameras a spatial resolution of a few micron has been achieved. Very high efficiency can be achieved in fiber optics plates with CsI scintillators, again coupled to CCDs. CsI can be grown in a column structure. The scintillation light is confined to the columns in a similar way as in fibers and is guided towards the sensor, which typically is a CCD, but can as well be a sensor of the MEDIPIX type. The spatial resolution is defined by the diameter of the columns, which can be as small as 10–20 μm .

5.3 The PIN Photodiode

The PIN photodiode is one of the simplest types of photodiodes. It is an intrinsic piece of high ohmic semiconductor sandwiched between two heavily doped n^+ and p^+ regions (Fig. 3.6). It is produced by standard semiconductor processes: boron diffusion on one side and phosphor diffusion on the other side of a high purity n -type silicon wafer. This configuration produces a field, which, even without an external field supplied, will tend to separate charges produced in the depleted region. The separated charges will be swept to the terminals and detected as current provided that they do not already recombine inside the semiconductor. The thick layer of intrinsic silicon (300 μm) reduces the capacitance of the diode and, thus, the serial noise, and makes it sensitive to red and infrared light, which has a rather long absorption length in silicon. Since this layer has a very low concentration of

Fig. 3.6 Structure of a PIN photodiode



dopants, only a small voltage is required to deplete the device completely. An additional advantage is the fact that the recombination/generation time constant is longest in case of undoped materials, which also provide a minimal thermal generation current. Clearly the top p-layer, which cannot be depleted, needs to be transparent to incoming light. A thin, but highly doped layer is used in silicon photodiodes.

The operation of a PIN photodiode is simple and reliable, but, since it has no internal gain, a charge sensitive amplifier and a low bandwidth filter amplifier are needed for the detection of low light level signals above the sizeable noise caused by the leakage current and the large diode capacitance, which is typically some 40 pF/cm^2 . On the other hand, due to the absence of internal gain, PIN photodiodes offer an exceptional stability. For the treatment of noise, we refer to [28]. The use of a charge-sensitive preamplifier and a filter amplifier makes the signal slow. The lowest intensity light flash detectable above noise needs to be several hundred photons for state of the art cm^2 PIN photodiodes and filter time constants of a few μs .

Nowadays, PIN diodes with areas of 10 cm^2 and more are available, and it is easy to manufacture position sensitive arrays—even monolithic ones—with a large number of elements. As mentioned before, the noise of large PIN photodiodes increases proportionally to the area, respectively to the diode capacitance.

The low signal-to-noise ratio requires long integration times in the electronics, reducing the ability to determine the arrival of the pulses, which is an important aspect for PET. Therefore, PIN photodiodes are generally not suitable for use in PET. In combination with PMTs PIN photodiodes have been used to measure the depth of interaction in a PET detector [29].

5.4 Silicon Drift Photodiode

If a low noise for a large area readout is required, a possible way out is drifting the photoelectrons to a small collection area with a low capacitance. A caveat is that the drift collection times can be quite long and again the readout will be rather slow; in addition, the flux has to be low to avoid pileup. The silicon drift photon detector (SDD) is a fully depleted diode in which an electric field nearly parallel to the

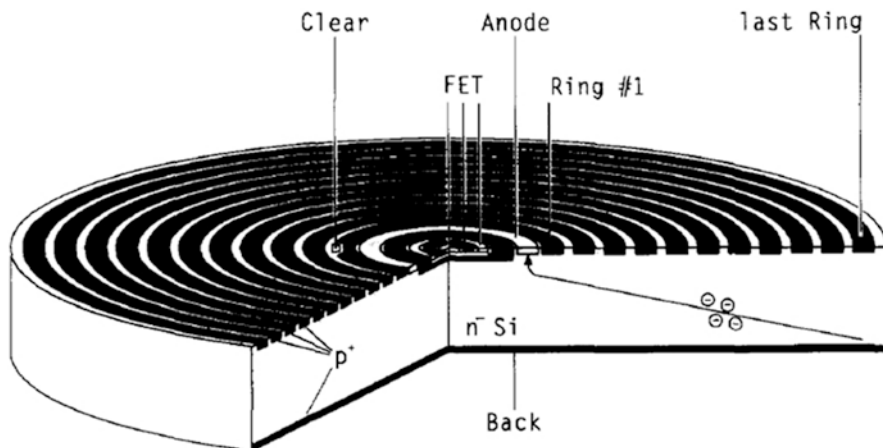


Fig. 3.7 Cross section of a cylindrical silicon drift detector with an integrated n-channel JFET. The entrance window is the non-structured backside. Reprinted with permission from [30]

surface is created by properly biased continuous field strips. Figure 3.7 shows a typical example. The field configuration drives free electrons created anywhere in the depleted volume towards a collecting anode in the center. The unique feature is a low noise due to an extremely low anode capacitance, which is, moreover, independent of the detector area. It is possible to achieve a noise level of only a few electrons, albeit with a jitter in time due to the normally unknown photon conversion location and thus due to the drift delay. To take full advantage of the low output capacitance, the front-end n-channel JFET of an amplifier can be integrated on the detector chip close to the n^+ implanted anode.

Examples for the excellent performance of these devices are given in [31, 32]. A circular SDD with an active area of 30 mm^2 has been coupled to the high light yield scintillator $\text{LaBr}_3(\text{Ce})$ and yielded an energy resolution of 2.7 % FWHM for the 662 keV line of ^{137}Cs when converted in the scintillator.

Gamma cameras of the Anger type with the excellent spatial resolution of 0.35 mm FWHM (Fig. 3.8) have been built [33] or are under construction [34].

6 Solid State Photon Detectors with Internal Amplification

6.1 Avalanche Photodiodes

A modification of the photodiode leads to a device known as the avalanche photodiode (APD). The APD is another step towards increasing the sensitivity of photon detectors by reducing the noise at high bandwidth. An avalanche photodiode (APD) is a p-n device with internal gain due to the high internal field at the

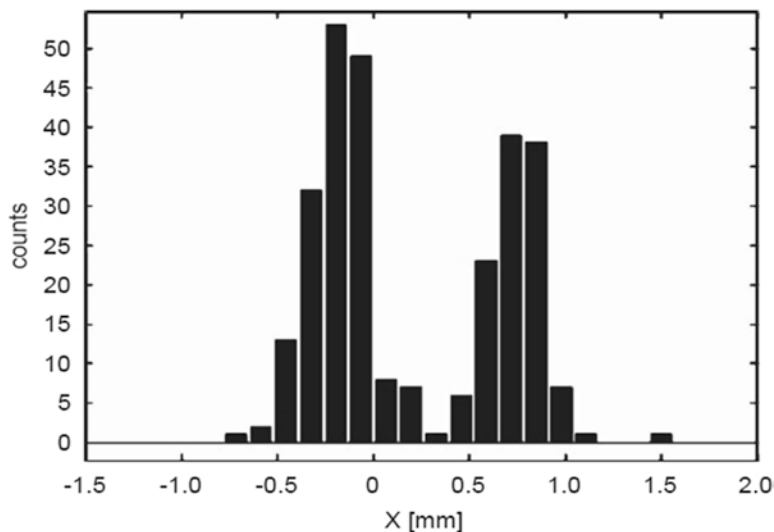


Fig. 3.8 One-dimensional section of two irradiation spots of a collimated ^{57}Co source. The average spatial resolution is 0.35 mm FWHM. Reprinted with permission from [33]

junction of positive and negative doped silicon. In an APD, a photoelectron in this field gains enough energy to create an electron–hole pair by impact ionization; both the initial electron and the additional electron again undergo high acceleration and can initiate further electron–hole pairs—thus starting an avalanche. The electric field must reach a critical value, called the impact ionization threshold, which is approximately 1.75×10^5 V/cm for silicon, before electrons can gain sufficient kinetic energy to generate electron/hole pairs [35]. The field strength for holes to generate impact ionization is around 2.5×10^5 V/cm [36]. The impact ionization process generates M additional carriers on average, where M is called the multiplication gain. The multiplication in practical APDs is moderate, between 50 and 200. A gain of 10^4 is in principle possible, but at gain values higher than a few hundred, the environment (e.g. temperature and voltage supply) needs to be strongly regulated because the APD has to be operated extremely close to the breakdown voltage.

Again, the QE is in the of 70–85 % range. When combined with the relative high gain, this leads to roughly equivalent performance for energy and timing compared with PMT-based detectors. APDs allow for a more compact PET scanner design, which together with the insensitivity of APDs to magnetic fields, makes it possible to place the detectors inside of a MRI magnet. Other design possibilities can be considered, for example multiple concentric rings of detectors (see Sect. 6.1.7), or the use of APD arrays on both front and back surfaces of scintillator arrays. Both these designs provide depth of interaction information.

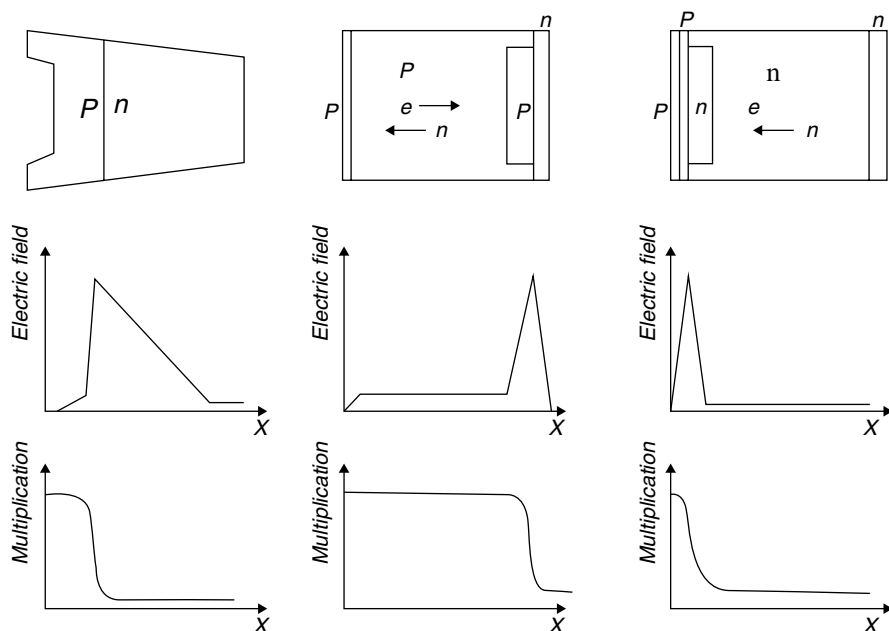


Fig. 3.9 Device structures, electric field profiles and electron/hole multiplication for (*left*) beveled-edge, (*center*) reach-through and (*right*) shallow junction APDs, modified from Webb et al. [37]

6.1.1 Structure of Common APDs

Commonly three alternative APD structures are used:

- Beveled-edge,
- Reach-through,
- Reverse or buried junction APD.

Here we discuss the p-on-n structures with a peak sensitivity in the ‘blue’ region. The n-on-p structure is basically a mirrored construction with highest sensitivity for red light.

The basic structure of these APDs is shown in the top row of Fig. 3.9, the electric field distributions as a function of depth for all three devices in the middle and the corresponding multiplication at the bottom. Electrons in both the beveled-edge and the reach-through structure have high multiplication rates throughout almost the entire device structure while hole multiplication is kept to a minimum. In the shallow junction APD (also called reverse APD), by contrast, photoelectrons must be generated in front of the p–n junction buried at a depth of a few microns to undergo multiplication. Full amplification can only be achieved when the diode is illuminated by blue light which has a very short absorption length of less than 1 μm .

Due to the production yield, the size of APDs is limited to achieve an extremely uniform field distribution over the sensitive area. The biggest area available commercially is 2.5 cm².

Advanced Photonix Inc. was the first to bring a large area APD on the market. The APDs have beveled edges to reduce the surface currents. It has a traditional p–n junction, in which the n-type resistivity is chosen such that it makes the breakdown voltage very high (~2,000 V). Due to a neutron transmutation process (the naturally occurring and uniform distributed ³⁰Si isotope is converted to P), the internal field and the gain are very uniform. Consequently, an excellent energy resolution of 4.3 % FWHM for the 662 keV line from ¹³⁷Cs has been measured with this so-called Large Area Avalanche Photo Diode (LAAPD) from Advanced Photonix in combination with a YAP:Ce crystal [38] and 3.7 % have been achieved in combination with a LaCl₃:Ce crystal [39]. The deep UV scintillation light of Argon (128 nm) has been detected with a LAAPD at a quantum efficiency greater than 40 % [40].

A reach-through APD has a wide low-field drift region (>100 μm) at the front of the device and the multiplying region at the back. Almost the full thickness is active. Since most of the thermally generated dark current inside the thick p layer undergoes electron multiplication, large area devices tend to be noisy.

The third type, the shallow junction APD has its p–n junction close to the front surface. An example is the APD developed for the CMS electromagnetic calorimeter [41].

The basic structure is low resistivity silicon with an epitaxial grown layer of low doped n-silicon on top. In this top layer with a thickness of 40–50 μm, the p–n junction is created by diffusion and ion implantation at a depth of ~5 μm. About 30–40 μm of the epitaxial grown layer of low doped n-silicon remains unaltered and acts only as a drift region. However, this reduces the capacitance and, consequently, the noise of the device. A groove close to the edge of the device prevents the flow of surface currents (Fig. 3.10).

The reverse APD has a number of advantages in PET applications:

- Fast response,
- Small dark current,
- Reduced temperature dependence.

6.1.2 Quantum Efficiency

The QE of a reverse APD is similar to the QE of a PIN photodiode (Fig. 3.5), but only photoelectrons created in front of the shallow p–n junction undergo full amplification while those produced close to the junction or behind see only part of the potential, and thus the amplification is reduced. The holes contribute little because they have a much smaller ionization coefficient than electrons at the same field strength. Photons with long wavelengths often penetrate deeper into the silicon (Fig. 3.11) and the photoelectrons have, therefore, less chance to undergo full amplification (Fig. 3.12) [42].

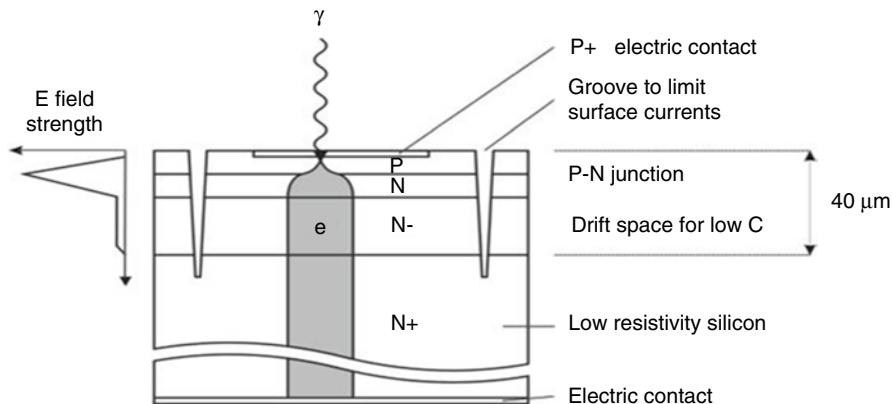


Fig. 3.10 Structure of the Hamamatsu S8148 APD used by CMS

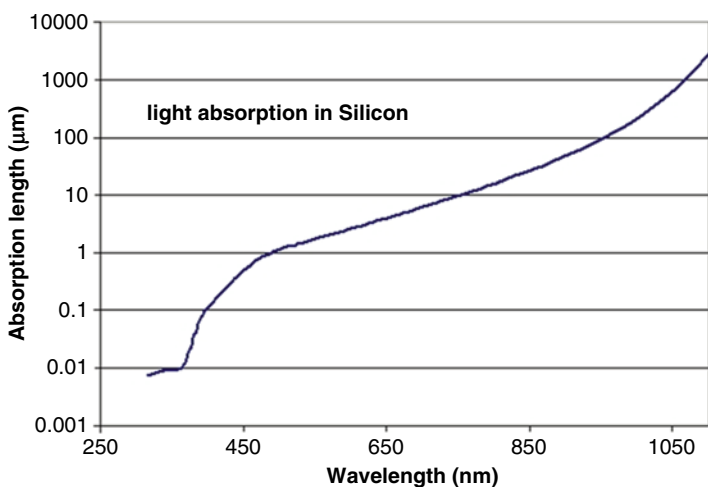


Fig. 3.11 The photon absorption length in μm of silicon versus wavelength [43]

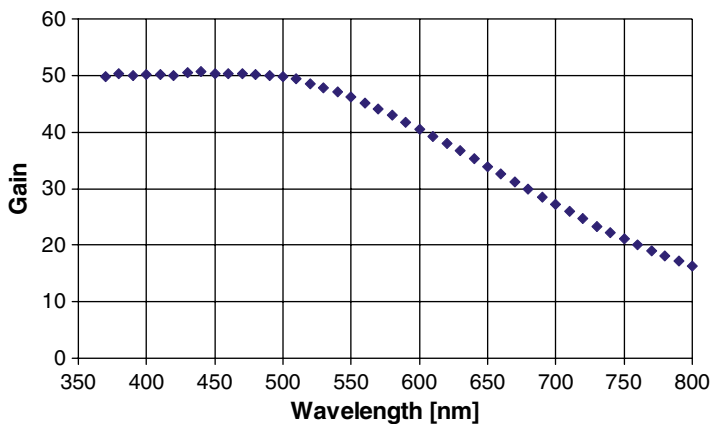


Fig. 3.12 Gain of a reverse type APD (Hamamatsu S8148) as a function of the wavelength of the incident light. Reprinted with permission from [42]

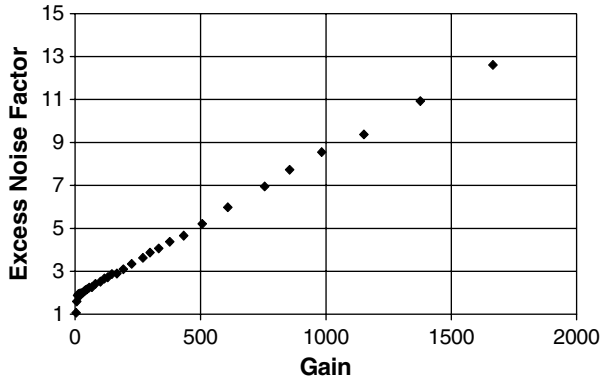


Fig. 3.13 Excess noise factor for different gains (Hamamatsu APD, type S8148). Reprinted with permission from [45]

State of the art crystal scintillators with elements with high atomic number (needed for PET because of best ratio of the photoelectric absorption to Compton scattering) have a peak light emission in the range of 350–500 nm, a range which is well covered by reverse APDs.

6.1.3 Excess Noise Factor

The avalanche multiplication in an APD is a stochastic process. The fluctuations are described by the excess noise factor F . In theory, it is at high gain (>10) mostly attributed to the contribution of the holes to the multiplication [44].

$$F = k_{\text{eff}} \cdot M + (2 - 1/M) \cdot (1 - k_{\text{eff}})$$

$$\text{for } M > 10 : F = 2 + k_{\text{eff}} \cdot M$$

$$k_{\text{eff}} \approx k = \beta/\alpha$$

α and β are the ionization coefficients for electrons and holes, $\alpha \gg \beta$ in APDs biased below breakdown.

The theoretical lower limit of F at small gain is 2. It increases linearly with the gain and is ~ 10 at a gain of 1,000 (Fig. 3.13).

6.1.4 Stability

The gain of an APD exponentially depends on the bias voltage and, therefore, the relative change of the gain with voltage is a linear function of the gain. At a gain of 50, the relative change is $\sim 3.1\%/V$ and increases linearly to more than $30\%/V$ at

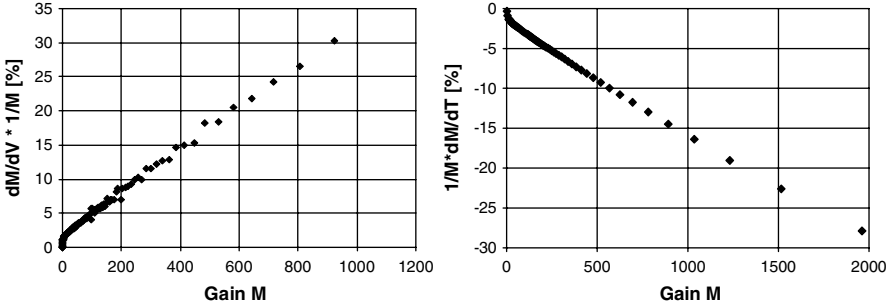


Fig. 3.14 Relative change of the gain for variations of the bias voltage (*left*) and the temperature (*right*) plotted as function of the gain for the Hamamatsu S8148. Reprinted with permission from [22]

gain 1,000. Similarly, the gain depends on temperature changes, which are caused by the energy loss in interactions of the electrons with phonons (Fig. 3.14). The relative change is ≈ 2.4 %/C at gain 100 and ≈ 15 %/C at gain 1,000 (Fig. 3.12, all values for the S8148 APD from Hamamatsu [22]). Because of the strong sensitivity to small changes in the bias voltage and temperature when operated close below the breakdown voltage, APDs have to be operated at moderate internal gain and need low noise preamplifiers.

6.1.5 Contribution of the APD Parameters to the Energy Resolution

In a scintillation detector with an APD as a readout element, the APD contributes to all three conventionally used terms describing the energy resolution:

$$\frac{\sigma_E}{E} = \frac{a}{\sqrt{E}} \oplus b \oplus \frac{c}{E}$$

In detail, APDs contribute to the stochastic term, a of the energy resolution of a crystal-APD system with their area (mismatch of the APD area and the crystal face), the quantum efficiency and the excess noise factor. The gain sensitivity to voltage and temperature variation increases the constant term b and the capacitance, serial resistance and dark current all add to the noise term c .

The dark current of state of the art APDs is very small and the excess noise factor is close to the theoretical limit as long as the gain is not too high. Therefore, the parallel noise (caused by the dark currents as shown in the first summand in the formula below) can only be improved by a short shaping time, which is anyhow needed in high rate calorimeters with state of the art scintillation crystals. Unfortunately, the short shaping time increases the series noise (caused by the capacitance of the APDs as shown in the second summand in the formula below), which becomes the dominant part. The APD should have the lowest possible

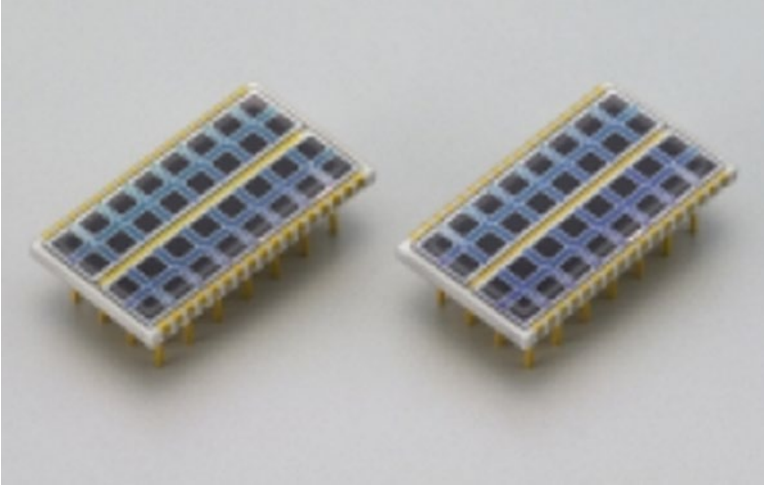


Fig. 3.15 Array of APDs from Hamamatsu with pixels of $1.6 \times 1.6 \text{ mm}^2$ and a pitch of 2.3 mm

capacitance to achieve the best possible energy resolution. To first order, the ENC is expressed by Eq. (17) from [46]:

$$ENC^2 \approx 2q \cdot \left(\frac{I_{ds}}{M^2} + I_{db} \cdot F \right) \cdot \tau + 4kTR_s \cdot \frac{C^2}{M^2} \cdot \frac{1}{\tau}$$

τ is the shaping time, q the electron charge, I_{ds} the dark surface current, I_{db} the dark bulk current created before the p–n junction, M is the gain, F the excess noise factor, R_s the series resistance of the APD and the amplifier input, C the capacitance of the APD and the amplifier input, k the Boltzmann constant, and T the absolute temperature.

6.1.6 Arrays of APDs

Arrays are available from several manufacturers for applications in nuclear medical imaging (SPECT and PET). An array with 32 reverse APDs, for example, is produced by Hamamatsu [47] specifically for small animal PET scanner design (Fig. 3.15). The area of the individual APDs is $1.6 \times 1.6 \text{ mm}^2$. Radiation Monitoring Devices (RMD) produces arrays with up to 169 reach-through APDs with an element size of $1 \times 1 \text{ mm}^2$ [48].

6.1.7 Examples of Small Animal PET Detectors Using APDs

In the following we will show some small animal PET examples, all using the new miniaturized photon sensors. Figure 3.16 shows the early prototype small animal PET named MADPET (Munich Avalanche Diode PET) using avalanche

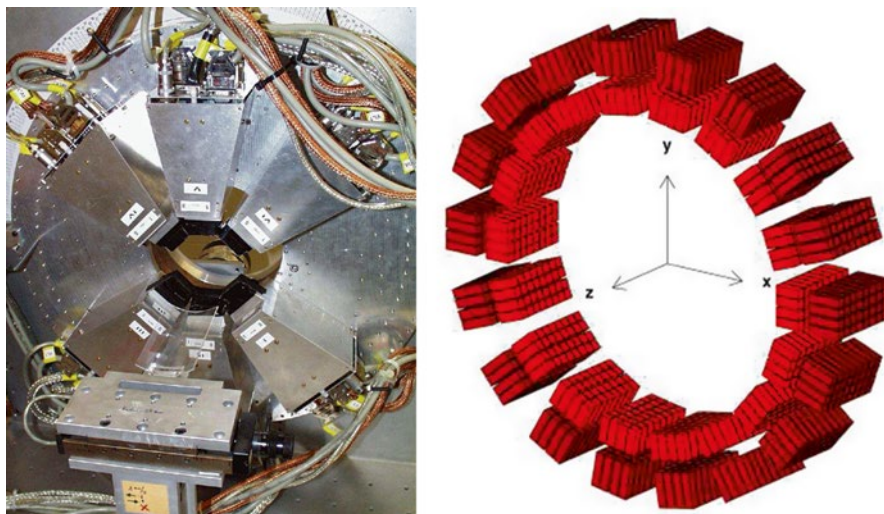


Fig. 3.16 MADPET with 48 detectors in 6 sectors (*left*) and arrangement of 1,152 crystals in MADPET II with two coaxial layers (*right*) with improved spatial resolution (<1.5 mm). Reprinted with permission from [49]

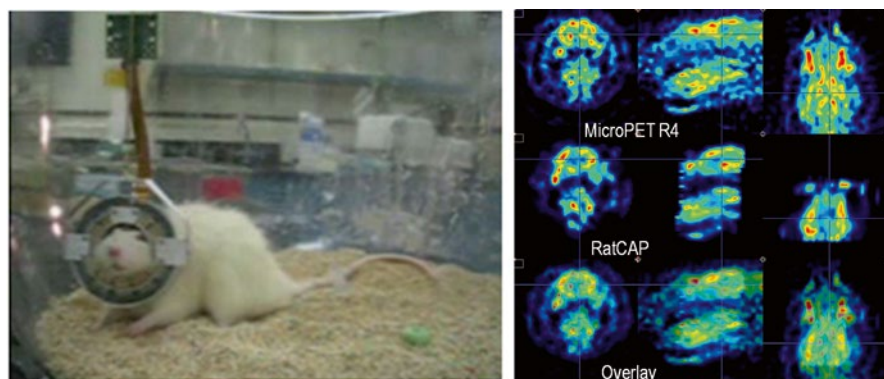


Fig. 3.17 *Left*: Awake rat wearing the RatCAP that is supported by the tether and mechanical counterbalance system. *Right*: ^{18}F -FDG rat brain images from the RatCAP compared to the same animal imaged with a MicroPET R4. *Vertical lines* show the axial coverage of the RatCAP. Reprinted with permission from [50]

photodiodes and its advanced version MADPET II, using the APD arrays shown in Fig. 3.15. The readout uses the 1:1 coupling. For reducing the parallax error the crystals in MADPET II were divided into two radial rings and read out separately, allowing for a resolution of less than 1.5 mm [49].

Figure 3.17 shows another design by Dr Woody et al., the so-called RatCAP, demonstrating clearly the potential of much more compact designs compared with those based on PMT readouts. A comparison with a measurement with the MicroPET R4 shows nearly the same resolution [50].

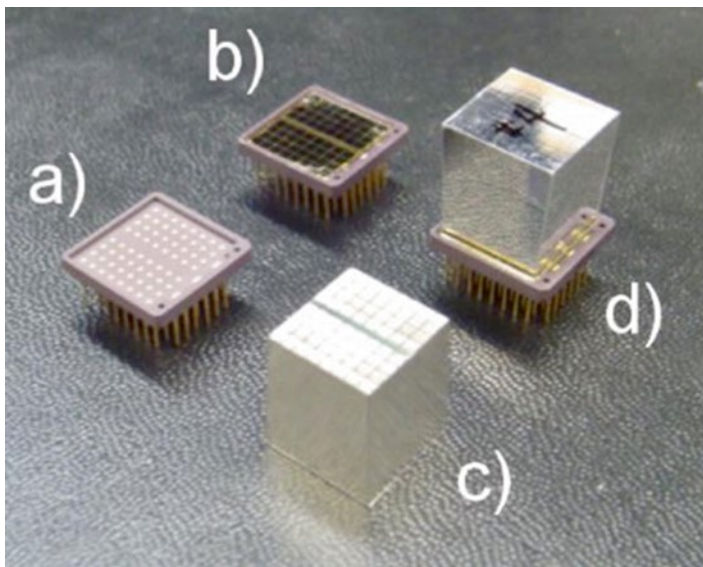


Fig. 3.18 Picture of: (a) ceramic case with bump bonding pads; (b) two APD arrays mounted in the ceramic; (c) custom tapered LYSO array; (d) assembled LabPET II module. Reprinted with permission from [51]

Dr Lecomte and co-workers were the first to realize a PET scanner with APD readout at Université de Sherbrooke in Canada. The most recent development which employs APDs is the LabPET II [51] shown in Fig. 3.18.

Also, the very compact design of APDs and their insensitivity to magnetic fields triggered the construction of first prototypes of combining MRI and PET. A PET–MRI combination for multimodality imaging was built in 2006/2007 at the University of Tuebingen (Fig. 3.19) for the simultaneously acquired images [52].

6.2 Geiger-Mode Avalanche Photodiodes

At the beginning of this millennium the Geiger-mode avalanche photodiode (G-APD) was developed. This device can detect single photons just like a PMT with a very high gain first dynode and therefore some people call it a ‘Silicon Photo Multiplier’ (SiPM). The pulse height spectrum measured with a G-APD shows a resolution even better than what can be achieved with the best hybrid photomultiplier tubes (Fig. 3.20). “Geiger-mode” describes the feature of these devices whereby a photo-generated carrier in the depletion region can trigger a diverging avalanche multiplication of carriers by impact ionization. Both positive and negative carriers (and also photons generated in the avalanche multiplication, see Sect. 6)

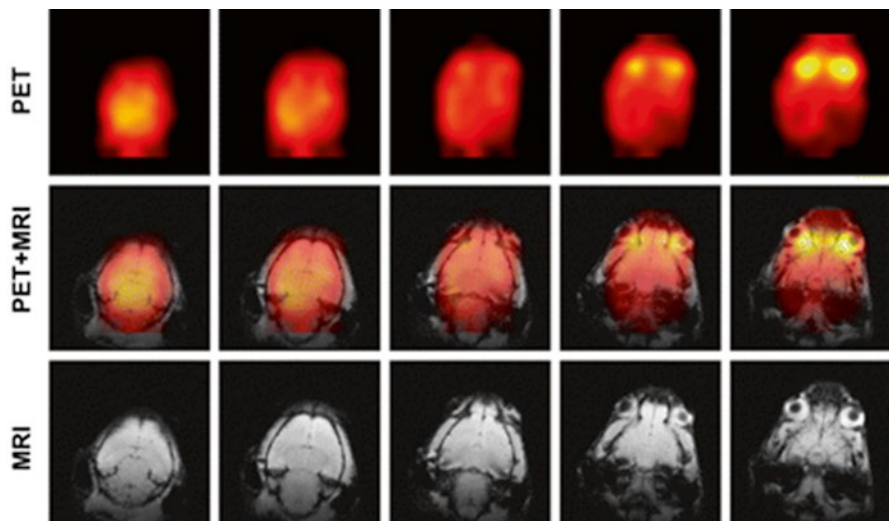


Fig. 3.19 Simultaneously acquired PET (filtered back projection, 2.5-mm Gaussian postsmoothing filter) and coronal unenhanced fast low-angle shot MRI (394/5.9, 40° flip angle, six signals acquired, 1-mm section thickness, 256×256 pixels) images of a mouse head injected with FDG. The fused PET/MRI images show good alignment of images acquired with the two imaging modalities. The increased uptake of the PET images correlates with the location of the Harderian glands behind the eyes in the MRI images. Reprinted with permission from [52]

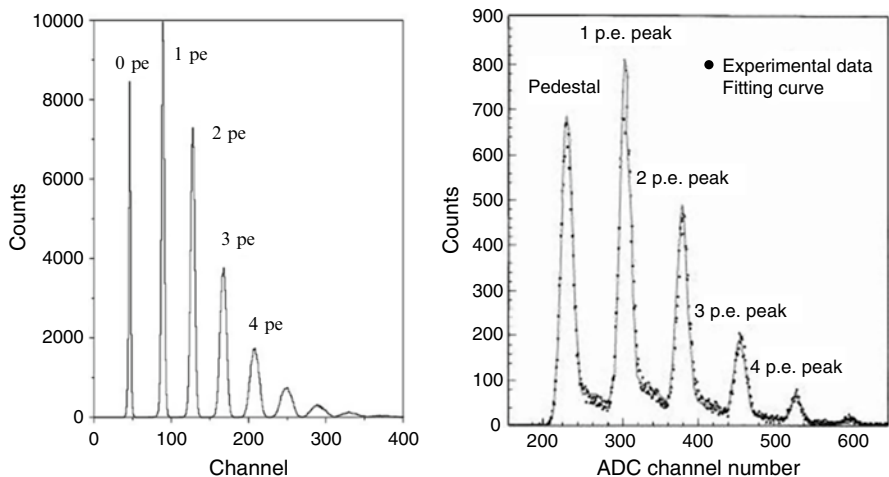


Fig. 3.20 Pulse height spectrum of light pulses with very low intensity recorded with a G-APD (left) and a HPD. Reprinted with permission from [53]

are involved with a positive feedback effect, which, when the electric field is high enough, makes the carrier multiplication self-sustaining. In linear mode APDs, avalanches develop basically only in one direction (from the p- towards the n-material) and stop multiplying when the charge carriers reach the low field area of the n-zone.

Very rarely secondary avalanches are started by holes or secondary photons in the p-layer. In G-APDs, the essential new process is the additional initiation of secondary avalanches, triggered by holes and secondary photons in the p-layer. A G-APD, therefore, does not turn off by itself and, as a consequence, the avalanche process must be quenched by the voltage drop across a high ohmic serial resistor or by an active quenching circuit. Another important feature of G-APDs is that it is possible to bias small depleted volumes at the p–n junction well over the so-called breakdown voltage much longer in time than on average a free electron is generated, which would lead to an avalanche breakdown, i.e. it is possible to keep small volumes for a sufficient amount of time in a ‘supercritical state’. It is obvious that large depleted volumes with a high electrical field could never be kept biased well over the breakdown voltage for a sufficiently long period because enough free electrons would always be thermally generated. Initially, the idea to ‘overbias’ small, single volumes was tried out in the 1970s of the last century [54, 55].

It is obvious that semiconductors of low band-gap (unless they are strongly cooled) or of high impurity will be completely unsuited for G-APDs because it is not possible to keep even very small depleted volumes free of charge carriers for sufficiently long periods of time. It is also obvious that materials with a high photon production (III–V materials for LED or laser diodes) are unsuited because, in the case of large secondary photon emission, secondary avalanches can be triggered in the entire ensemble of small cells by optical crosstalk.

6.2.1 History

Pioneering work in the development of solid state single photon detectors, biased above the breakdown voltage, was carried out in the 1960s of the last century in the RCA company by R.J. McIntyre and coworkers [54] and by R.H. Haitz and his colleagues in the Shockley research laboratory [55]. The main problem was that only very small volumes of Si could be kept depleted for sufficient time above breakdown voltage to keep the diodes sensitive for photons. In most cases, the high internal bulk current in the depleted volume triggered an instant breakdown when the diode bias rose just above the breakdown voltage. Due to improved technologies it was possible to keep the depleted volume free of electrons biased well above breakdown for a sufficiently long time. The development led to the so-called Single Photon Avalanche Diode (SPAD).

Around 1990, the MRS (metal–resistor–semiconductor) APDs were invented in Russia. A very thin metal layer (Ti, $\sim 0.01 \mu\text{m}$) and a layer of SiC or Si_xO_y with a resistivity of 30–80 M Ω cm limits the Geiger breakdown by a local reduction of the electric field. The technology is complicated because all parameters need to be controlled very precisely. The next step was logical: subdivide the MRS structure into many cells and connect them all in parallel by an individual limiting resistor (Fig. 3.21). The Geiger-mode avalanche photodiode (G-APD) was born. Key personalities in this development were Golovin [56] and Sadygov [57]. The G-APD is produced by a standard MOS (metal–oxide–silicon) process and promises to eventually be relatively simple and therefore cheap.

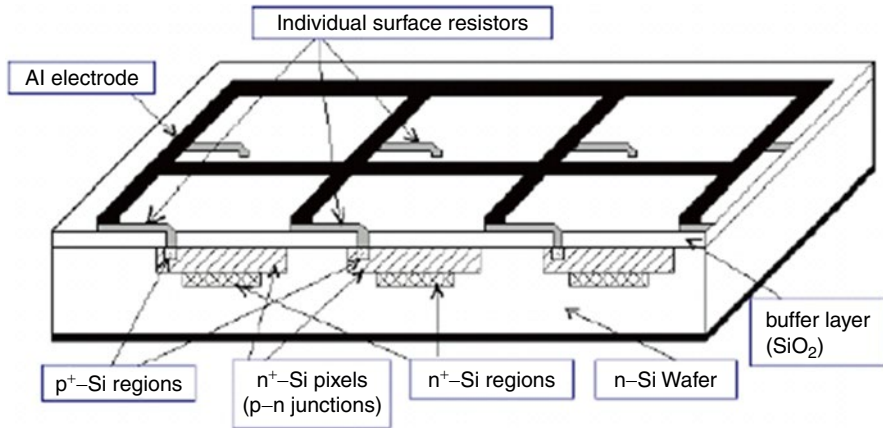


Fig. 3.21 Basic structure of a Geiger-mode avalanche photodiode. Reprinted with permission from [57]

6.2.2 Properties of G-APDs

High Gain

G-APDs produce a standard signal when any of the cells goes to breakdown. The amplitude A is proportional to the capacitance of the cell divided by the electron charge times the overvoltage:

$$A_i \sim C/q \cdot (V - V_b)$$

where V is the operating bias voltage and V_b is the breakdown voltage.

When many cells are fired at the same time, the output is the sum of the standard pulses

$$A = \sum A_i$$

In this way the basically digital device has a linear response. The gain is typically in the range of 10^5 – 10^7 but there are also designs with a gain of only 10^4 (see later discussion). Single photons produce a signal of several millivolts on a 50Ω load (Fig. 3.22).

No (or at most a simple) amplifier is needed for many applications for single photon detection. Particularly low-level light detection with PIN photodiodes or linear mode APDs requires high quality shielding to prevent pickup. Because of the extremely small extension of the cell size and the high gain, G-APDs have practically no pickup noise and often need no shielding at all. Since there are no avalanche fluctuations as in normal APDs, the excess noise factor is very small and it could eventually be negligible if other contributions from optical crosstalk could be suppressed. Groom's theorem [58] is not valid. This theorem states that the

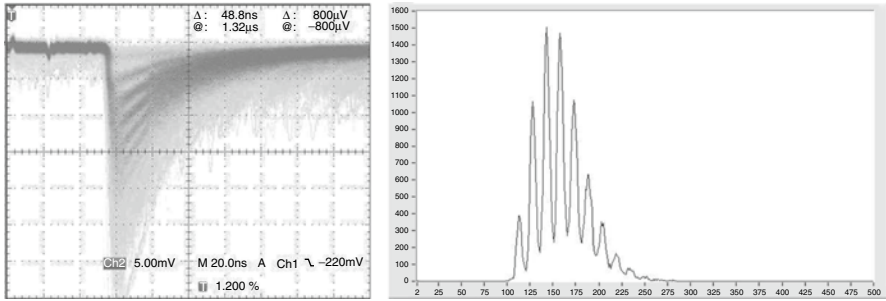
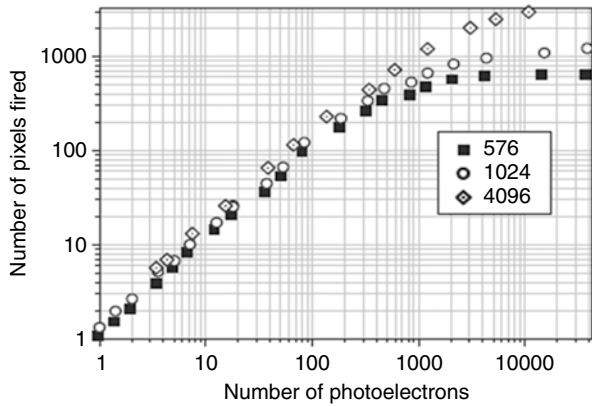


Fig. 3.22 *Left:* Oscilloscope picture of the signal from a G-APD (Hamamatsu 1-53-1A-1) recorded without an amplifier. *Right:* The corresponding pulse height spectrum. The mean number of photons in the recorded light flashes is about 2.5. Horizontal scale in arbitrary units

Fig. 3.23 Nonlinear response to a 40 ps laser light signal for G-APDs with different number of cells. Reprinted with permission from [59]



resolution of an assembly of a scintillator and a semiconductor photon detector is independent of the area of the photon detector because, in first order, the photon statistic improves linearly with the photon detector area while equally the noise increases linearly with the detector capacitance, which is again proportional to the area.

Saturation in Case of Bright Light Flashes

The output signal is proportional to the number of fired cells as long as the number of photons in a pulse (N_{photon}) times the PDE is significantly smaller than the number of cells N_{total} (Fig. 3.23). The equation given below is not exact but describes the data very well.

$$A \approx N_{\text{firedcells}} = N_{\text{total}} \cdot \left(1 - e^{-\frac{N_{\text{photon}} \cdot \text{PDE}}{N_{\text{total}}}} \right)$$

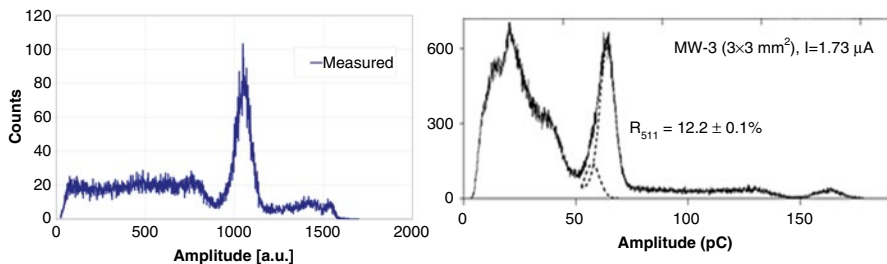


Fig. 3.24 *Left:* Energy spectrum measured with a ^{22}Na sources and a LYSO crystal ($2 \times 2 \times 12 \text{ mm}^3$) coupled to a G-APD from CPTA/Photonique with $\sim 400 \text{ cells/mm}^2$. *Right:* LYSO of the same size and a G-APD from Zecotek with $15,000 \text{ cells/mm}^2$

Two or more photons which convert within the same time in one cell produce exactly the standardized signal of 1 single photon. When the number of impinging photons times the PDE exceeds 50 % of the available cells, the deviation from linearity becomes more than 20 %. When a spectrum of the response of a scintillator and G-APD detector is measured the nonlinear response acts as a compression and fakes an energy resolution which looks better than it is in reality.

In PET, SPECT applications this is not a severe disadvantage provided the dynamic compression is not too high and easy calibration is possible. G-APDs with a very large number of cells (up to $40,000 \text{ cells/mm}^2$) have been produced and are available from Zecotek Photonics Inc. Fig. 3.24 highlights the deviation from linearity when observing a ^{22}Na source with a crystal read out by a G-APD with 400 cells/mm^2 and with a G-APD of $15,000 \text{ cells/mm}^2$.

Sensitivity of the Gain to the Bias Voltage Stability

The G-APD signal stability depends mainly on (a) the stability of the applied bias and (b) on temperature changes (see next section). To describe the dependence of the G-APD response on the bias voltage one can introduce a voltage dependent coefficient $k_V(V)$ as follows:

$$k_V(V) = \frac{1}{A} \cdot \frac{dA}{dV} \cdot 100\%$$

Examples of the voltage dependence are shown in Fig. 3.25. The amplitude A of the signals of 2 G-APDs from Hamamatsu and Photonique/CPTA have been measured and the coefficients derived [60].

For precision measurements, the voltage has to be regulated at the diode and not before the bias resistor, to avoid gain drops due to large temporary light signals, resulting in current changes in the resistor and, in turn, a voltage drop.

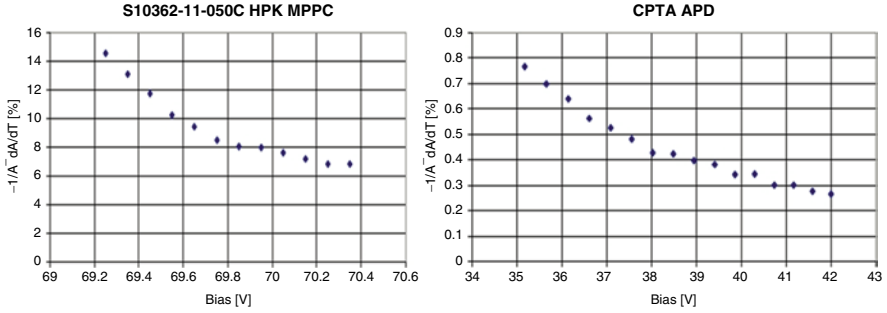


Fig. 3.25 Voltage coefficients $k_V(V)$ of a G-APD from Hamamatsu (*left*) and from Photonique/CPTA (*right*) depending on the bias voltage at $T=22^\circ\text{C}$. Reprinted with permission from [60]

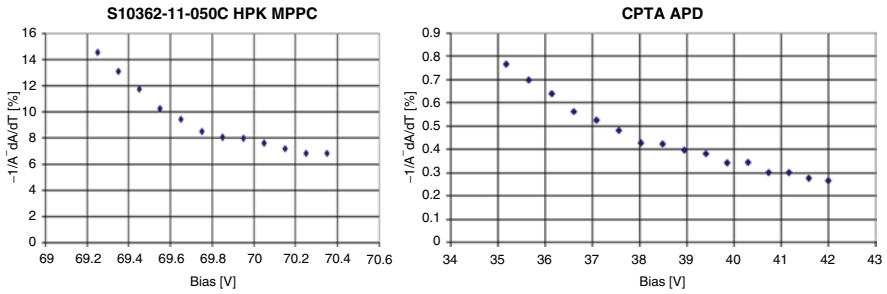


Fig. 3.26 Temperature coefficients of a G-APD from Hamamatsu (*left*) and from Photonique/CPTA (*right*) as a function of the bias voltage. Reprinted with permission from [60]

Temperature Dependence of the Gain

The breakdown voltage of a silicon diode depends strongly on the temperature because of the interactions of the carriers with phonons. Almost all parameters of a G-APD are a function of the overvoltage $V-V_b$. Here we discuss the influence of temperature changes on the gain. Similar to the coefficient $k_V(V)$, which describes the dependence on the bias voltage, we define

$$k_T(V) = \frac{1}{A} \cdot \frac{dA}{dT} \cdot 100\%$$

Again, the amplitudes A of the signals of 2 G-APDs from Hamamatsu and Photonique/CPTA were measured at different temperatures and the coefficients derived (Fig. 3.26) [60].

For a stable operation, the temperature needs to be controlled with a precision of a fraction of a degree. Alternatively, the applied bias voltage has to be corrected to compensate for the shift of the breakdown voltage caused by temperature changes.

For the device from Hamamatsu, the bias voltage needs to be increased by ~ 50 mV when the temperature rises by 1 °C and if the device is operated with at least a $V_{OV} > 1$ V, while for the Photonique/CPTA device the compensation of bias voltage is ~ 20 mV/°C for $V_{OV} > 1$ V.

Photon Detection Efficiency (PDE)

The PDE is the product of (a) the quantum efficiency (QE) of the active area, (b) the geometric fill factor ε (ε = ratio of sensitive to total area), and (c) the probability that an incoming photon triggers a breakdown (P_{trigger}). A small correction for the hit cell still recovering from a previous breakdown (from noise or a previous light signal) is neglected in the current discussions

$$\text{PDE} = \text{QE} \cdot \varepsilon \cdot P_{\text{trigger}}$$

The geometric factor ε needs to be optimized depending on the application. Since some space is needed between the cells for separation and the individual resistors, the best filling can be achieved with a small number of big cells, and a geometric fill factor of 80 % or more is possible. A pixel with cells of large size generally has the disadvantage of a low dynamic range and of a larger number of periods of insensitivity due to the accumulation of cells in the recovery phase caused by the more frequent noise triggers in the larger depleted volume.

G-APDs for SPECT and PET need a large number of cells for unit area. One of the preferred materials for PET nowadays, Lutetium Oxyorthosilicate (LSO) crystals, produce many photons ($\approx 15,000$ per a 511 keV) and up to a few 1,000s can be collected at the end face of the crystals. To avoid saturation effects, the number of cells needs to be big for the given viewing area and, in turn, the cells must be small. The currently achieved geometric fill factor ε in suitable models is in the range of 40–60 %. An example is shown in Fig. 3.27.

The triggering probability depends on the position where the primary electron–hole pair is generated. Compared to holes, electrons have a better chance to trigger a breakdown in silicon. Therefore, a conversion of the photon in the p-layer has the highest probability to trigger a breakdown. This has been calculated by Oldham et al. [61]. They define an avalanche region with a width W and the position x , which runs from 0 to W starting at the n-edge (Fig. 3.28).

Oldham and coworkers verified their calculations by illuminating a diode with short (390 nm) and long (1,050 nm) wavelengths and achieved good agreement.

G-APDs with an n-on-p structure (sketch in the right pane of Fig. 3.28) operated just above the breakdown voltage V_b are inefficient for short wavelength photons because these photons must penetrate into the p layer to generate electrons that initiate avalanches when moving towards the n-layer (see Fig. 3.11 for the absorption length of photons in silicon). When raising the voltage well above V_b , holes generated by short wavelength photons in the n-layer will be able to initiate a measurable signal. According to Fig. 3.28, a much higher overvoltage is required for obtaining

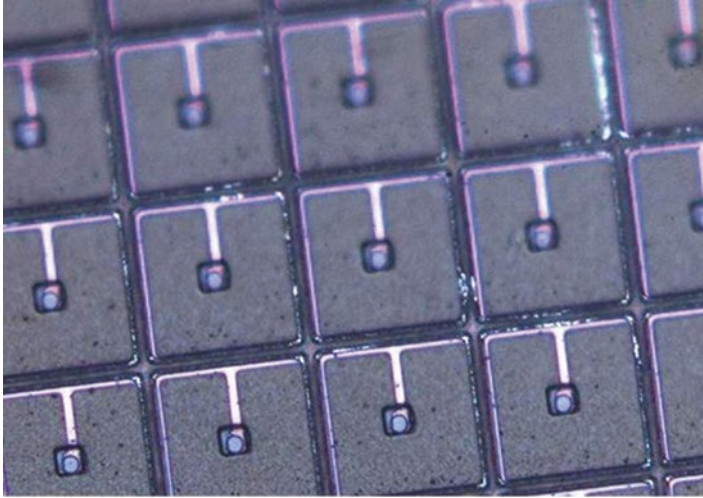


Fig. 3.27 Magnified photo of a G-APD produced by Photonique/CPTA

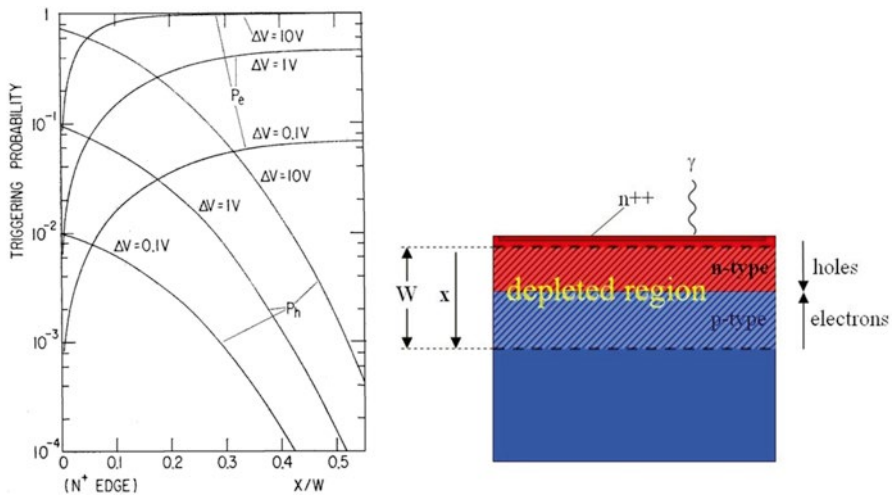


Fig. 3.28 Triggering probability for different positions of carrier generation (left, see text, modified [61]) and sketch of the structure for an explanation of the parameters W and x (right)

a reasonable blue-sensitivity of n-on-p structures compared to that required in the case of a p-on-n structure.

The QE of the active area can reach 80–90 % depending on the wavelength. It peaks in a relatively narrow range of wavelengths compared to the QE distribution of a PIN diode (Fig. 3.29) because the sensitive layer of silicon is very thin. In the case shown in Fig. 3.29, the G-APD structure is p-silicon on an n-substrate. The p-layer is $0.5 \mu\text{m}$ thick on a $4 \mu\text{m}$ epitaxial n-layer.

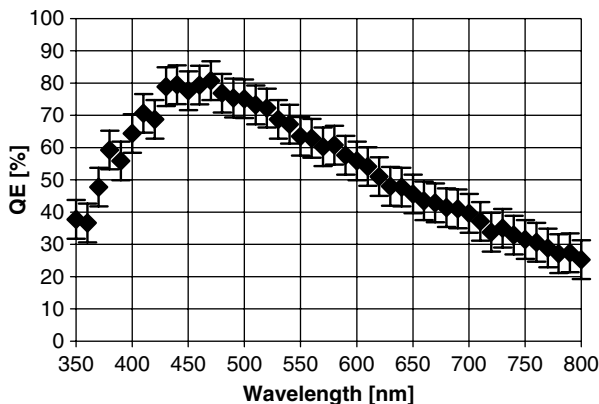


Fig. 3.29 Quantum efficiency of the active area as a function of the wavelength for Hamamatsu 0-50-2 with 400 cells/mm². The error bars denote the systematic measuring errors. The unpublished measurements shown in this figure and in Fig. 3.30 have been done by Y. Musienko [INR (Moscow) and Northeastern University (Boston)], and some in the following figures without a reference (Figs. 3.32, 3.33, and 3.35) by D. Renker

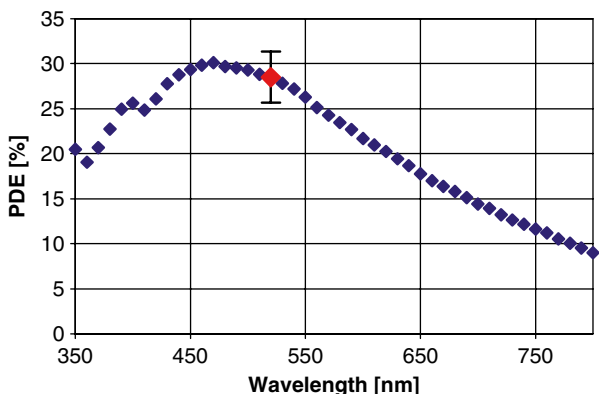


Fig. 3.30 PDE of a so-called p-on-n G-APD produced by Hamamatsu (PSI-33-050C) operated 1 V over the breakdown voltage. The red data point with error bars indicates the size of the systematic error

The overall PDE is shown in Fig. 3.30 for a blue sensitive device (p-on-n structure) for the detection of scintillation light from crystals used in PET (BGO, LSO or LaBr₃), and in Fig. 3.31 for a device with the inverted n-on-p structure useful together with CsI(Tl) in SPECT.

The PDE depends on the overvoltage (Fig. 3.32). Operation at high gain (high bias voltage) is favored but, in most cases, a compromise needs to be found because at high gain the dark currents and the dark count rate become very high and the optical crosstalk increases.

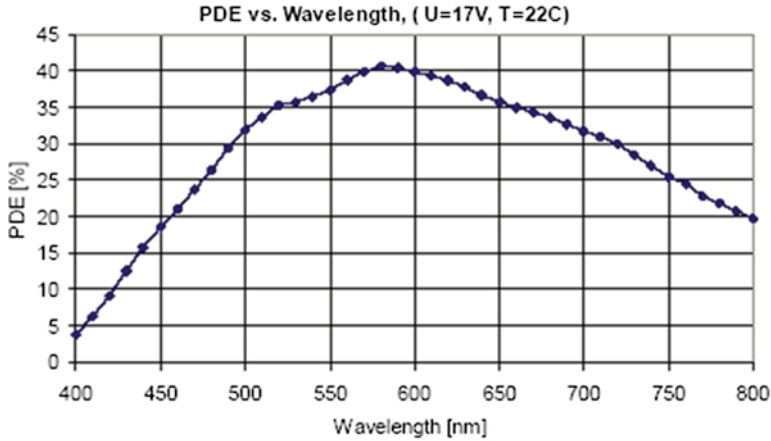


Fig. 3.31 PDE of an n-on-p G-APD produced by Photonique/CPTA (SSPM_0710G9MM) operated about 4 V over the breakdown voltage [62]

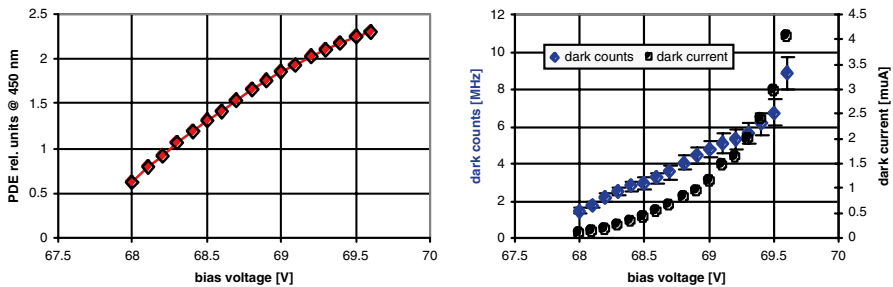


Fig. 3.32 PDE of Hamamatsu MPPC-33-050C as a function of the applied bias voltage in relative units (*left pane*) and the dark currents and dark counts measured at 25 °C in the same voltage range (*right pane*)

Dark Counts

A breakdown can be triggered by an incoming photon or by any generation of free carriers in the depleted layer of a few micron thickness. The latter produces dark counts with a rate of 100 kHz to several MHz per mm² at 25 °C and with a threshold at half of the one photon amplitude (Fig. 3.32). Two main processes are responsible for dark counts, thermally generated e–h pairs and so-called field-assisted generation of free electrons.

Thermally generated free carriers can be reduced by cooling. There is a factor 2 reduction of the thermally generated dark counts with every 8 °C drop in temperature.

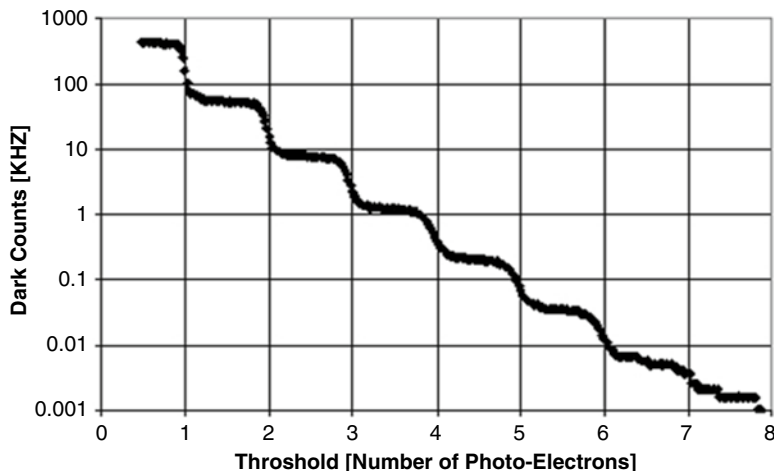


Fig. 3.33 Dark count rate for different values of the discriminator threshold. The G-APD used in this measurement is the S10362-11-050C from Hamamatsu operated at a gain of 7.5×10^5

Field-assisted generation without the help of a phonon (trap-assisted tunneling [63, 64]) has, compared to the thermal generation, a relatively small effect. It can only be reduced by operating the G-APDs at a smaller electric field, thereby lowering the gain and reducing the PDE.

In medical imaging inorganic crystals with a high light yield are used and the dark counts are not giving cause for concern because the number of recorded events falls rapidly with a high setting of the threshold.

Optical Crosstalk

In an avalanche breakdown, there are on average three photons emitted per 10^5 carriers with a photon energy higher than 1.14 eV, the band gap of silicon [65]. When these photons travel to a neighboring cell they can trigger a breakdown there like any external photon. This effect is called optical crosstalk. It can be visualized in the dark count distribution shown in Fig. 3.33. An avalanche from a dark count can, by optical cross talk, occasionally trigger a few additional cells to fire.

The optical crosstalk acts like shower fluctuations in an APD. It is a stochastic process and introduces an excess noise factor F as in a normal APD or in a PMT. Neglecting saturation effects and contributions from afterpulses and dark counts in the wide gate needed for the measurement of light from a scintillating crystal F can be approximated:

$$F \approx 1 + p_{ct}$$

The probability p_{ct} is defined by the rate of dark count events with crosstalk (threshold 1.5 fired cells) divided by the total dark count rate (threshold 0.5 fired cells).

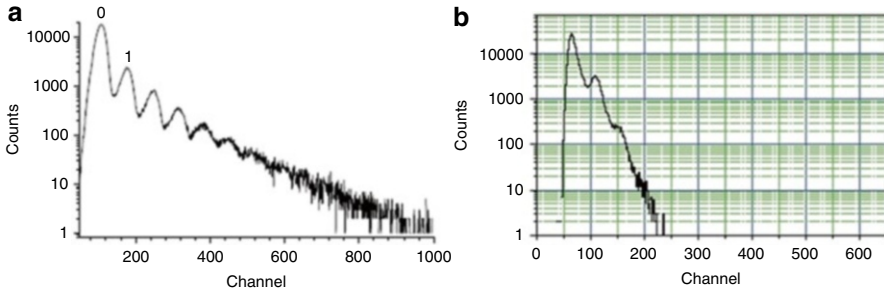


Fig. 3.34 Optical crosstalk in a $1 \times 1 \text{ mm}^2$ G-APD produced by MEPHI/Pulsar, measured as the dark count pulse height distribution: no suppression (a); with suppression of the optical crosstalk (b) by grooves. Reprinted with permission from [67]

With a dedicated design, which has an additional junction and with grooves between the cells acting as an optical isolation, the optical crosstalk can be reduced [66–68]. The effect of grooves is highlighted by the change in the dark count pulse height spectrum shown in Fig. 3.34. Operation at relatively low gain is advantageous for reducing optical crosstalk, albeit with the disadvantage of significantly reducing the PDE. A quite convenient alternative method of suppressing optical crosstalk is inserting narrow grooves between cells and filling them with an optical absorber. The disadvantage is the need for space reducing the active area, i.e. reducing the fill factor ϵ and, in turn, the PDE.

A concern in compact scintillator-G-APD arrangements is the fact that photons generated in a breakdown of a G-APD penetrate into a crystal that is coupled to the G-APD, are then reflected at the end of the crystal and come back to the G-APD where some additional cells might be triggered. This effect was simulated by a reflector made of aluminized Mylar, which was mounted in front of a G-APD from Hamamatsu (type PSI-11-100C operated at a gain of 2.4×10^6) to simulate the emission into a crystal and reflection of the light at the other end of the crystal.

The peaks from dark counts with internal cross talk (two or more cells fired) were enhanced by $\sim 18\%$ (from 15.7% crosstalk probability to 18.6%) by reflected photons (Fig. 3.35). With a diffuse reflector (eight layers of Teflon foil) the enhancement was $\sim 12\%$.

Afterpulsing

In the silicon volume where a breakdown happened, a plasma with high temperatures (a few $1,000^\circ\text{C}$) is formed and deep-lying traps in the silicon are filled. Carrier trapping and delayed release causes afterpulses during a period of several 100 ns after a breakdown.

The afterpulse probability of the device Hamamatsu S10362-33-050C was measured by counting dark counts in a gate with a fixed width but variable delay (Fig. 3.36). Two components were found with a 50 and 140 ns time constant, respectively [69].

Fig. 3.35 Spectrum of dark count events with and without a reflector made of aluminized Mylar in front of a G-APD (Hamamatsu PSI-11-100C) operated at a gain of 2.4×10^6

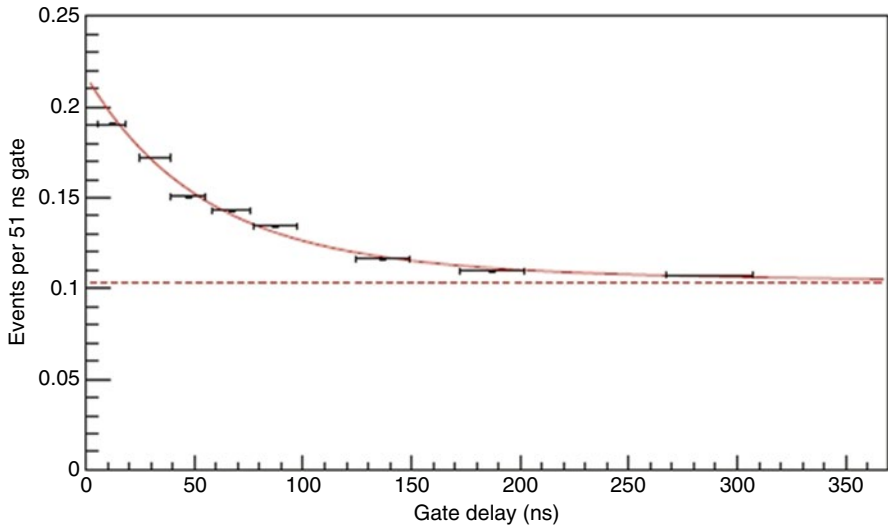
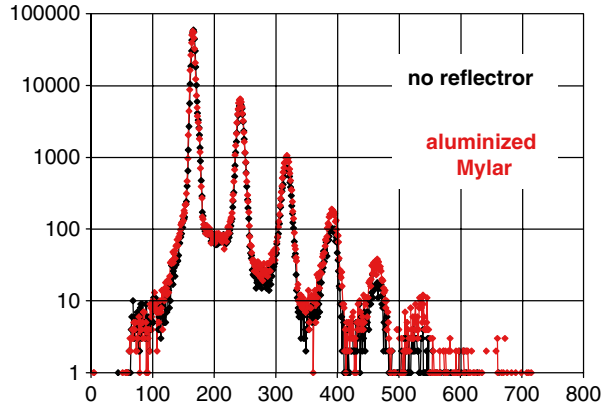


Fig. 3.36 The probability for a delayed release of carriers as a function of time after a breakdown event. The level of dark counts is indicated by the *dashed line*. Reprinted with permission from [69]

Scintillator-G-APD detectors need rather long electronic integration times (200 ns and more). Therefore the afterpulses contribute to the output signal. Since this is a stochastic process the afterpulses contribute to the excess noise factor in a way similar to the optical crosstalk.

Recovery Time and Pulse Shape

The time needed to recharge a cell after a breakdown has been quenched depends mostly on the cell capacitance and the individual quenching resistor ($\tau \sim RC$). Afterpulses can prolong the recovery time, because the recharging starts anew.

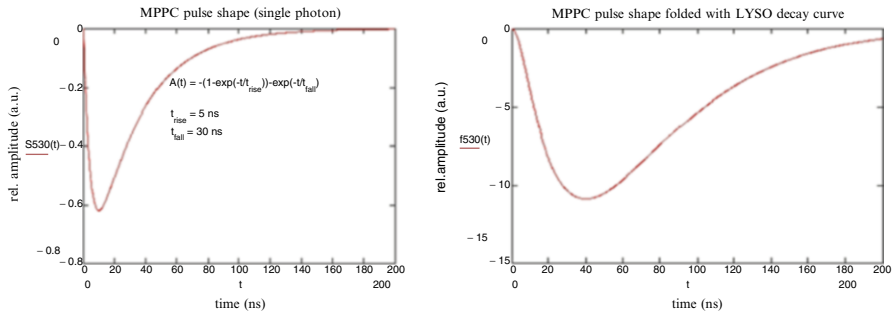


Fig. 3.37 Pulse shape of a G-APD from Hamamatsu (S10362-330050C) for single photons (*left*) and for photons from a LYSO crystal with a decay time of 40 ns (*right*). Reprinted with permission from [70]

Some G-APDs need hundreds of microseconds after a breakdown until the amplitude of a second signal reaches 95 % of the first signal. The shortest recovery times is found in G-APDs with small cells and small resistors. State of the art devices (for example Hamamatsu S10362-33-050) have a recovery time of less than 50 ns (see Fig. 3.37 left). A short recovery time is crucial because the saturation effect is enhanced when many cells are in a recovery state.

The recharging of the cells defines the fall time of the signals, which is the same as the recovery time. When a G-APD is coupled to a scintillating crystal like lutetium–yttrium–oxyorthosilicate (LYSO), the rise time of the signals can become quite long (see Fig. 3.37, right). This can be explained by a convolution of the G-APD signal fall time with the time distribution of the photon emission of the LYSO scintillation [70].

Timing

The active layer of silicon in a G-APD is very thin (2–4 μm) and the process of the breakdown development is fast. In addition, the signal amplitude is large because of the high cell capacitance. Therefore, very good timing properties even for single photons can be expected. Fluctuations in the avalanche development are mainly due to a lateral spreading by diffusion and by the photons emitted in the avalanche [71, 72]. The vertical avalanche build-up contributes only little to the timing. Figure 3.38 shows a measurement of the time response of a G-APD in the case of single photon triggers [53]. The authors state a 40 ps contribution from both the used laser and the electronics. The result, then, is a time resolution with a standard deviation of 42 ps. Operation at high overvoltage (high gain) improves the time resolution.

The time resolution of PET detectors based on LYSO crystals and G-APDs is dominated by the spread of the arrival time of the scintillation photons at the entrance window of the G-APD caused mainly by the variation in path length in the crystal with a high index of refraction ($n = 1.82$). With two types of G-APDs, the so-called

Fig. 3.38 Time resolution for single photons. Reprinted with permission from [53]

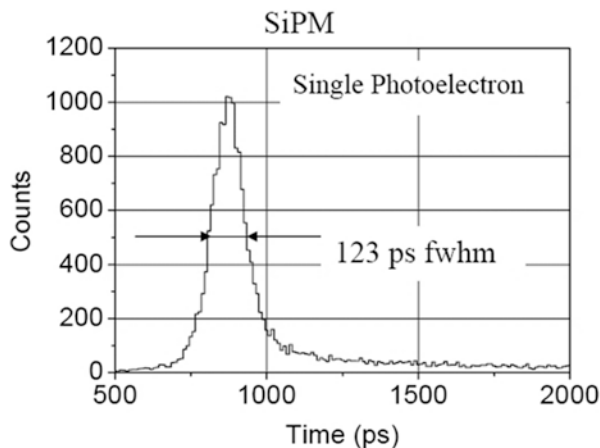
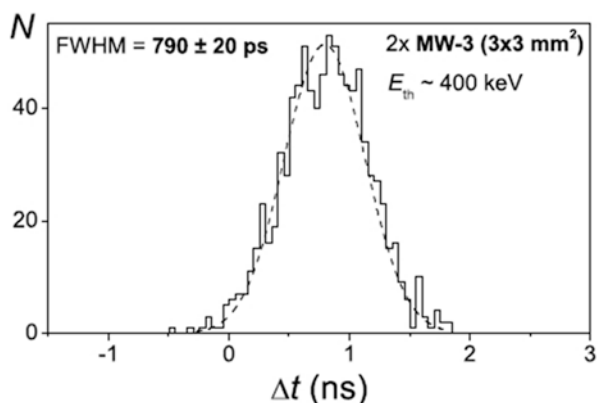


Fig. 3.39 Time difference between the signals from two identical detectors made of LYSO ($2 \times 2 \times 12 \text{ mm}^3$) coupled to G-APDs at the registration of two 511 keV γ -quanta emitted simultaneously at 180° from a ^{22}Na source positioned between the detectors. The dashed line is a Gaussian fit to the data. Reprinted with permission from [74]



SiPM produced in MEPHI/Pulsar and the MW-3 produced by Zecotec Photonics, similar time resolutions of about 800 ps have been measured [73, 74]. Figure 3.39 shows an example of such a measurement.

Radiation Hardness

G-APDs have been irradiated with ionizing radiation (^{60}Co) and started to show damage effects at doses of about 200 Gy. This is several orders of magnitude more than the dose that can be expected in SPECT or PET even in a long operation period of 10 years. For medical application G-APDs can be considered as radiation hard.

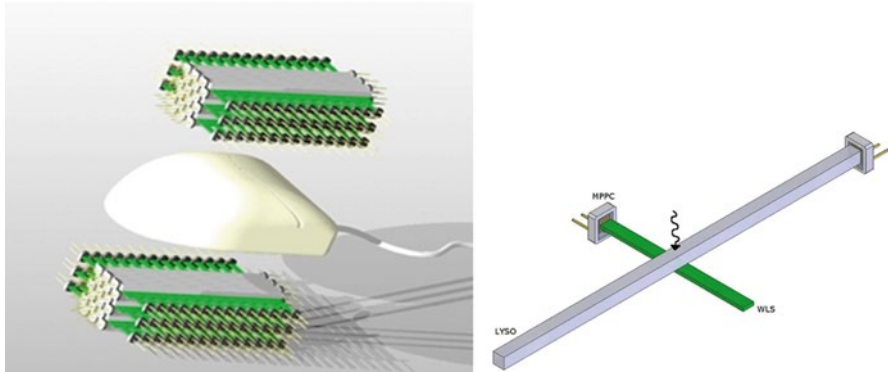


Fig. 3.40 Sketch of the principle and the building components (LYSO crystal, WLS strips and readout by G-APDs)

6.3 *Examples of Some Detectors Using G-APDs as Readout Sensors*

As G-APDs are still in the developmental phase, nuclear medical instruments using G-APDs are rather sparse. Currently, the efforts concentrate on PET developments and on the proof of concept demonstrators for small animal imaging devices. The two main drawbacks are the much higher price per unit of sensitive area compared to PMTs, and the requirement to wait for maturity of the device before starting on the design of large detectors for human medical applications. On the other hand, the development of small animal imaging devices is an excellent training ground for what might be achieved later in large scale production. In the following we briefly mention two developments, the AX-PET and a development pursued at the University of Tuebingen.

The AX-PET is a novel concept for a 3-D axial PET geometry [75]. It allows for a new way of measuring the interaction point in the detector with very high precision. Figure 3.40 shows the basic concept of the AX-PET. It is based on a matrix of long LYSO crystals oriented in the axial direction, each coupled to one G-APD array. To derive the axial coordinate, WLS (Wave Length Shifter) strips are mounted orthogonally and interleaved between the crystals. The light from the WLS strips is read by custom-made G-APDs. The weighted mean of the signals in the WLS strips has proven to give a very precise axial position information. The achievable resolution along the three axes is mainly driven by the dimensions of the LYSO crystals and WLS strips. This concept is inherently free of parallax errors. Furthermore, it will allow identification of most Compton interactions in the detector and reconstruction of a fraction of them, which is expected to enhance image quality and sensitivity.

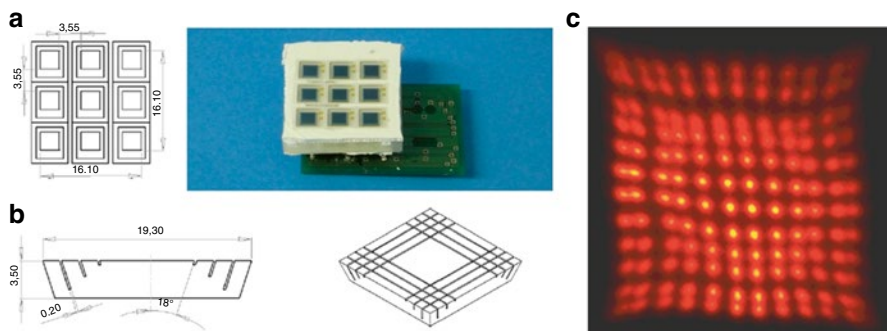


Fig. 3.41 Detector components (**a**: the G-APD array and a photograph of the array, **b**: the projection of the light guide and configuration of cuts) and (**c**) first result of the crystal map

The results are [75]:

- Energy resolution: 11.5 % FWHM @ 511 keV
- High achieved light collection and accordingly a large number of photo electrons created in the G-APD ($\sim 1,000$ pe @511 keV)
- Axial spatial resolution: 1.1 mm FWHM

The second example is a study of the block detector concept for reading out a matrix of 144 small LSO crystal bars, $1.5 \times 1.5 \times 10$ mm³ each, by only 9 G-APDs [76]. It was decided to use 9 G-APDs instead of only four for the block readout concept, because the currently largest available commercial G-APDs have an area of only 3×3 mm. By using simple summing amplifiers the signals of the 9 G-APDs were reduced to only four signals. The matrix was coupled by means of a simple and not yet optimised light guide to the G-APDs, which cover only $\approx 29\%$ of the crystal block end face. Figure 3.41 shows the basic elements and the achieved crystal map. The mean energy resolution achieved over the entire block was 24 % (FWHM) and the averaged timing resolution 0.96 ns. The group also tested the influence of a strong magnetic field by placing such a detector inside a MRI magnet. Nearly no degradation of performance was observed, i.e. it was confirmed that such a block readout could be used for a PET–MRI simultaneous acquisition.

7 Additional Comments

In this section, we to briefly mention some rather special issues beyond the main function of photon sensors.

7.1 A Comment on Photon Sensor Costs

Photon sensor costs are now a major factor in the entire imaging device: in the typical component chain: scintillator crystals → photon detectors → electronics → readout, the photon detector development is progressing at slowest speed. Better crystal quality as well as a reduction of prices has been seen in recent years. The production of better, cheaper and more complex electronics with a higher potential of integration is progressing fastest. The performance of data storage and computing power is doubling nearly by a factor 2 within 18 months. Not following the trend are the costs of photon sensors. The unit price for the active area of a G-APD is still between factors 10 and 100 higher than that of PMTs. The high price prevents rapid progress and, in turn, the commercialisation of cost effective small animal imaging devices.

7.2 Integration of Electronics onto the Semiconductor Photon Sensors

Semiconductor photon sensors bear another potential. Extrapolating a few years into the future it is quite likely that step by step the control electronics (bias control, temperature control...) and later the signal processing electronics (amplifiers, summing amplifiers, digital electronics for the trigger, etc.) will be integrated on the same chip. The potential for linear mode APDs is much lower than that for the G-APDs because of quite disjunctive production methods and much higher operation voltage. As G-APDs production methods are close to the MOS technology it is a natural path towards integrating electronics on the same chip by MOS technology (preferentially by the high voltage MOS production procedure).

7.3 The Trend Towards Multimodal Imaging

In small animal imaging one would also prefer to simultaneously retrieve physiological and morphological data in coincidence, i.e. by combing for example CT with PET or MRI with PET. Particularly the increase in special resolution can only be fully used if one knows the morphological structure in the time of data acquisition. Especially the combination of MRI and PET should soon be realisable, because the interference of a PET detector using miniature semiconductor photon sensors and an MRI installation would be minimal except for a small reduction of the FoV inside the MRI magnet. Therefore, the need of combining PET and MRI will be a strong driving force to further improve solid state photon detectors. While the proof of concept has already been demonstrated last year for linear mode APD readout, the first demonstration of using the more robust G-APDs will very likely happen within late 2009 or 2010. The combination of CT and PET will be more complex because of the incoherence of the detection processes.

8 Outlook

Photon detectors are an essential element in nearly all modern small animal imaging detectors. The usual strong need to miniaturise detectors and to improve their performance, as well as the need to reduce costs, nowadays results in intense developments for replacing the classical workhorse of past times for PET and SPECT, the PMT, by solid-state photon detectors. Developments concentrate on G-APDs for both PET and SPECT and very soon detectors combing PET and MRI will be available, first as prototypes and a few years later as commercial products. The main drive behind such a development is the large step in miniaturisation on the photo sensor size and the insensitivity to magnetic fields. It will take at least 2–4 years until G-APDs will have reached a high level of maturity.

In the typical component chain: scintillation crystals → photon detectors → electronics → readout the photon detector development is progressing with the slowest speed. The developments for CT sensors are going on with even slower speed. What is missing is a persuading idea of how to change from analogue readout to a simpler, high rate digital readout, which might allow one to reduce the very high radiation load by about a factor 10 without spoiling the resolution.

In the following years we might expect some major improvements in G-APDs produced on other indirect semiconductor materials with a higher bandgap than that of Silicon, the successive integration of electronics onto the semiconductor photon sensor chip moreover the production of large monolithic matrices of G-APDs for coupling to crystal matrices of fine pixelisation. Figure 3.42 shows a first monolithic matrix of 8×8 G-APDs.

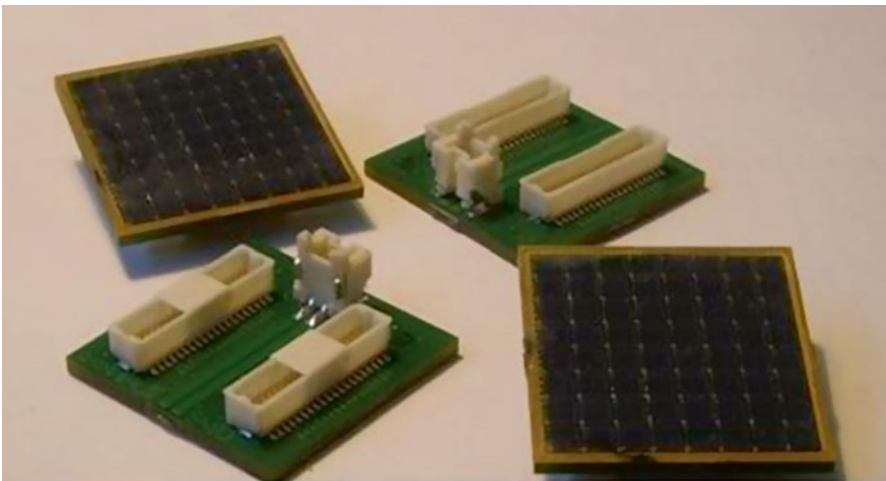


Fig. 3.42 8×8 Arrays of Geiger-mode APDs produced by Zecotek Photonics Inc

Acknowledgements Herewith we would like to thank many of our colleagues for comments and useful suggestions. We also thank Sybille Rodriguez for corrections and formatting the chapter.

References

1. A. Einstein (1905) Über einen die Erzeugung und Verwandlung des Lichtes betreffenden heuristischen Gesichtspunkt, *Ann Physik* **322**: 132-148.
2. W.W. Moses and S.E. Derenzo (1993) Empirical observation of performance degradation in positron emission tomographs utilizing block detectors, *J Nucl Med* **34**: 101P.
3. M. Watanabe, H. Uchida, H. Okada et al. (1992) A high resolution PET for animal studies, *IEEE Trans Med Imaging* **11**: 577-580.
4. P.D. Cutler, S.R. Cherry et al. (1992) Design features and performance of a PET system for animal Research, *J Nucl Med* **33**: 595-604.
5. P.M. Bloomfield, S. Rajeswaran, T.J. Spinks et al. (1995) The design and physical characteristics of a small animal positron emission tomography, *Phys Med Biol* **40**: 1105-1126.
6. K. Wienhard, M. Dahlbohm, L. Eriksson et al. (1994) The ECAT EXACT HR: Performance of a new high resolution positron scanner, *J Comput Assist Tomogr* **18**: 110-118.
7. K. Wienhard, M. Schmand, M.E. Casey et al. (2002) The ECAT HRRT: performance and first clinical application of the new high resolution research tomography, *IEEE Trans Nucl Sci* **49**: 104-110.
8. P. Bruyndonckx, X. Liu, S. Tavernier and Z. Shuping. (1997) Design and physical characteristics of a small animal PET using BaF₂ crystals and a photosensitive wire chamber, *Nucl Instr Meth Phys Res A* **392**: 407-413.
9. S.R. Cherry, Y. Shao, R.W. Silverman et al. (1997) MicroPET: a high resolution PET scanner for imaging small animals, *IEEE Trans Nucl Sci* **44**: 1161-1166.
10. A. Del Guerra, G. Di Domenico, M. Scandola and G. Zavattini (1998) High spatial resolution small animal YAP-PET, *Nucl Instr Meth A* **409**: 537-541.
11. M. Watanabe, H. Okada, K. Shimizu et al. (1997) A high resolution animal PET scanner using compact PS-PMT detectors, *IEEE Trans Nucl Sci* **44**: 1277-1282.
12. Y.C. Tai, A.F. Chatzioannou, Y. Yang et al. (2003) MicroPET II: design, development and initial performance of an improved microPET scanner for small-animal imaging *Phys Med Biol* **48**: 1519-1537.
13. T. Tomitani, N. Nohara, H. Muramaya et al., (1985) Development of a high resolution positron CT for animal studies, *IEEE Trans Nucl Sci* **32**: 822-825.
14. R. Lecomte, J. Cadorette, S. Rodrigue et al. (1996) Initial results from the Sherbrooke avalanche photodiode positron tomography, *IEEE Trans Nucl Sci* **43**: 1952-1957.
15. A.P. Jeavons, R.A. Chandler and C.A.R. Dettmar (1999) A 3D HIDAC-PET camera with sub-millimetre resolution for imaging small animals, *IEEE Trans Nucl Sci* **46**: 468-473.
16. S.E. Derenzo, R.H. Huesman, J.L. Cahoon et al. (1988) A positron tomograph with 600 BGO crystals and 2.6 mm resolution, *IEEE Trans Nucl Sci* **35**: 659-664.
17. R. Lecomte, C. Martel and J. Cadorette (1991) Study of the resolution performance of an array of discrete detectors with independent readouts for positron emission tomography, *IEEE Trans Med Imaging* **10**: 347-357.
18. R.S. Miyaoka, S.G. Kohlmyer and T.K. Lewellen (2001) Performance characteristics of micro crystal element (MiCE) detectors, *IEEE Trans Nucl Sci* **48**: 1403-1407.
19. J. Elster and H. Geitel (1889) Einige Demonstrationsversuche zum Nachweis einseitiger Elektrizitätsbewegung in verdünnten Gasen bei Anwendung glühender Elektroden, *Ann. Physik*, **274**: 27-39.
20. V.K. Zworykin and J.A. Rajchman (1939) The electrostatic electron multiplier, *Proc. IRE* **27**: 558-566.

21. http://sales.hamamatsu.com/assets/pdf/catsandguides/UBA_SBA_TPMH1305E03.pdf
22. D. Renker (2002) Properties of avalanche photodiodes for applications in high energy physics, astrophysics and medical imaging, *Nucl Instr Meth A* **486**: 164-169.
23. P. Fischer (1996) An area efficient 128 channel counter chip, *Nucl Instr Meth A* **378**: 297-300.
24. R. Ballabriga et al. (2007) The Medipix3 prototype, a pixel readout chip working in single photon counting mode with improved spectrometric performance, *IEEE Trans Nucl Sci* **54**: 1824-1829.
25. M. Locker et al. (2004) Single photon counting X-ray imaging with Si and CdTe single chip pixel detectors and multichip pixel modules, *IEEE Trans Nucl Sci* **51**: 1717-1723.
26. C. Broennimann et al. (2006) The PILATUS 1 M detector, *J Synchrotron Rad* **13**: 120-130.
27. A. Bergamaschi et al. (2007) Experience and results from the 6 Megapixel PILATUS system, *Proc. 16th International Workshop on Vertex detectors*, Lake Placid, NY, USA, 2007, paper PoS(Vertex 2007)049.
28. V. Radeka (1987) Semiconductor detectors and readout electronics: Present directions and outstanding problems: An introduction to the symposium *Nucl Instr Meth A* **253**: 309-312.
29. W.W. Moses, S.E. Derenzo, C.L. Melcher, R.A. Manente (1995) A room temperature LSO/PIN photodiode PET detector module that measures depth of interaction, *IEEE Trans Nucl Sci* **42**: 1085-1089.
30. P. Lechner et al. (1996) Silicon drift detectors for high resolution room temperature X-ray spectroscopy, *Nucl Instr Meth A* **377**: 346-351.
31. C. Fiorini et al. (2006) Gamma-ray spectroscopy with LaBr₃Ce scintillator readout by a Silicon drift detector, *IEEE Trans. Nucl. Sci.* Vol. **53**: 2392-2397.
32. M. Moszynski et al. (2009) A comparative study of Silicon drift detectors with photomultipliers, avalanche photodiodes and PIN photodiodes in gamma spectroscopy with LaBr₃ crystals, *IEEE Trans Nucl Sci* **56**: 1006-1011.
33. C. Fiorini et al. (2009) Imaging performances of the DRAGO gamma camera, *Nucl Instr Meth A* **604**: 101-103.
34. C. Fiorini et al. (2008) Silicon Drift Detectors arrays for the HICAM gamma camera, 2008 IEEE NSS Conference Record, pp. 2981-2983.
35. R.J. McIntyre (1999) A new look at impact ionization-Part I: A theory of gain, noise, breakdown probability, and frequency response, *IEEE Trans Elec Dev* **46**: 1623-1631.
36. C.A. Lee et al. (1964) Ionization rates of holes and electrons in Silicon, *Phys Rev A* **134**: 761-773.
37. P. P. Webb, R. J. McIntyre and J. Conradi (1974) Properties of avalanche photodiodes, *RCA Review*, Vol. 35, pp. 234-278.
38. M. Moszynski et al. (2000) Large Area Avalanche Photodiodes in X-rays and scintillation detection, *Nucl. Instr. and Meth. A* **442**: 230-237.
39. C.P. Allier et al. (2002) Readout of a LaCl₃(Ce³⁺) scintillation crystal with a large area avalanche photodiode, *Nucl Instr Meth A* **485**: 547-550.
40. R. Chandrasekharan et al. (2006) Detection of VUV light at high quantum efficiency with large area avalanche photodiodes (LAAPDs), *Nucl Instr Meth A* **567**: 45-47.
41. K. Deiters et al. (2000) Properties of the most recent avalanche photodiodes for the CMS electromagnetic calorimeter, *Instr Meth. A* **442**: 193-197.
42. Th. Kirm et al. (1997) Wavelength dependence of avalanche photodiode (APD) parameters, *Nucl. Instr. Meth. A* **387**: 202-204.
43. K. Rajkanan, R. Singh and J. Shewchun (1979) Absorption coefficient of silicon for solar cell calculations, *Solid-State Electronics* **22**: 793-795.
44. R.J. McIntyre (1972) The distribution of gains in uniformly multiplying avalanche photodiodes: Theory, *IEEE Trans Elec Dev* **19**: 703-713.
45. K. Deiters et al. (2001) Investigation of the avalanche photodiodes for the CMS electromagnetic calorimeter operated at high gain, *Nucl Instr Meth A* **461**: 574-576.

46. V. Radeka (1968) Optimum signal-processing for pulse-amplitude spectrometry in the presence of high-rate effects and noise, *IEEE Trans Nucl Sci* **15**: 455-470.
47. http://sales.hamamatsu.com/assets/pdf/parts_S/S8550.pdf
48. <http://www.rmdinc.com/products/p006.html>
49. Ziegler, S. (2005) Positron Emission Tomography: Principles, Technology and Recent Developments, *Nucl Phys A* **752**: 679-687.
50. C. Woody et al. (2007) Initial studies using the RatCAP conscious animal PET tomograph, *Nucl Instr Meth A* **571**: 14-17.
51. Ph. Berard et al. (2009) Development of a 64-channel APD detector module with individual pixel readout for sub-millimeter spatial resolution in PET, *Nucl Instr Meth A* **610**: 20-23.
52. M. Judenhofer et al. (2007) PET/MR Images Acquired with a compact MR-compatible PET Detector in a 7-T Magnet, *Radiology* **244**: 807-814.
53. P. Buzhan et al. (2003) Silicon photomultiplier and its possible applications, *Nucl Instr Meth A* **504**: 48-52.
54. R.J. McIntyre (1961) Theory of Microplasma Instability in Silicon, *J Appl Phys* **32**: 983-995.
55. R.H. Haitz. (1964) Model for the electrical behavior of a microplasma, *J Appl Phys* **35**: 1370-1376.
56. V. Golovin (1999) Avalanche Photodetector, Russian Agency for Patents and Trademarks, Patent No. RU 2142175.
57. Z. Sadygov (1998) Avalanche Detector, Russian Agency for Patents and Trademarks, Patent No. RU 2102820.
58. D.E. Groom (1984) Silicon photodiode detection of bismuth germanate scintillation light, *Nucl Instr Meth* **219**: 141-148.
59. V. Andreev et al. (2005) A high-granularity scintillator calorimeter readout with silicon photomultipliers, *Nucl Instr Meth A* **540**: 368-380.
60. Y. Musienko et al. (2007) Tests and performance of multipixel Geiger mode APD's and APD's for the CMS ECAL, *Proc. of Science (PD07)* 012.
61. W.G. Oldham et al. (1972) Triggering phenomena in avalanche diodes, *IEEE Trans Elec Dev* **19**: 1056-1060.
62. http://www.photonique.ch/Prod_0710G9MM.html
63. G.A.M. Hurkx et al. (1992) A new recombination model for device simulation including tunneling, *IEEE Trans Elec Dev* **39**: 331-338.
64. G.A.M. Hurkx et al. (1992) A new analytical diode model including tunneling and avalanche breakdown, *IEEE Trans Elec Dev* **39**: 2090-2998.
65. A. Lacaita et al. (1993) On the bremsstrahlung origin of hot-carrier-induced photons in silicon devices, *IEEE Trans Elec Dev* **40**: 577-582.
66. N. Basharuli et al. (2002) Registration of charged particles by scintillating fibers coupled with micro-cell Si APD, *Advanced Technology and Particle Physics*, World Scientific, Singapore, pp. 627-632.
67. P. Buzhan et al. (2006) Large area silicon photomultipliers: Performance and applications, *Nucl. Instr. Meth. A* **567**: 78-82.
68. W.J. Kindt (1999) Geiger mode avalanche photodiode arrays for spatially resolved single photon counting, PhD Thesis, Delft University Press, The Netherlands.
69. Th. Kraehenbuehl (2008) G-APD arrays and their use in axial PET modules, Diploma thesis, ETH Zuerich, Switzerland.
70. Ch. Casella et al. (2008) Readout of a LYSO crystal with MPPCs. Calculations and measurements of the signal shape, AX-PET note 2008-001.
71. A. Lacaita et al. (1990) Observation of avalanche propagation by multiplication assisted diffusion in *p-n* junctions, *Appl Phys Letters* **57**: 489-491.
72. A. Lacaita et al. (1993) Photon-assisted avalanche spreading in reach-through photodiodes, *Appl Phys Letters* **62**: 606-608.
73. P. Buzhan et al. (2006) Timing by silicon photomultiplier: A possible application for TOF measurements, *Nucl. Instr. Meth. A* **567**: 353-355.

74. I. Britvitch et al., (2006) Study of avalanche microchannel photodiodes for use in scintillation detectors, 2006 JINST 1 P08002
75. E. Bolle et al. (2008) A demonstrator for a new axial PET concept, IEEE Nuclear Science Symposium Conference Record, 2008, pp 4571-4571.
76. A. Kolb, E. Lorenz, M.S. Judenhofer, D. Renker, K. Lankes, B.J. Pichler, 2010. Evaluation of Geiger-mode APDs for PET block detector designs. *Phys Med Biol* **55**: 1815-1832.